

Online Deep Equilibrium Learning for Regularization by Denoising

Jiaming Liu^{1,*}, Xiaojian Xu^{2,*}, Weijie Gan²,
Shirin Shoushtari¹, and Ulugbek S. Kamilov^{1,2}

¹Department of Electrical and Systems Engineering, Washington University in St. Louis, MO 63130, USA

²Department of Computer Science and Engineering, Washington University in St. Louis, MO 63130, USA

Abstract

Plug-and-Play Priors (PnP) and Regularization by Denoising (RED) are widely-used frameworks for solving imaging inverse problems by computing fixed-points of operators combining physical measurement models and learned image priors. While traditional PnP/RED formulations have focused on priors specified using image denoisers, there is a growing interest in learning PnP/RED priors that are end-to-end optimal. The recent Deep Equilibrium Models (DEQ) framework has enabled memory-efficient end-to-end learning of PnP/RED priors by implicitly differentiating through the fixed-point equations without storing intermediate activation values. However, the dependence of the computational/memory complexity of the measurement models in PnP/RED on the total number of measurements leaves DEQ impractical for many imaging applications. We propose ODER as a new strategy for improving the efficiency of DEQ through stochastic approximations of the measurement models. We theoretically analyze ODER giving insights into its convergence and ability to approximate the traditional DEQ approach. Our numerical results suggest the potential improvements in training/testing complexity due to ODER on three distinct imaging applications.

1 Introduction

There has been considerable recent interest in using *deep learning (DL)* in the context of imaging inverse problems (see recent reviews [1–3]). Instead of explicitly defining a regularizer, the traditional DL approach is based on training a *convolutional neural network (CNN)* architecture, such as U-Net [4], to invert the measurement operator by exploiting the natural redundancies in the imaging data [5–9]. *Plug-and-Play Priors (PnP)* [10] and *Regularization by Denoising (RED)* [11] are two well-known alternative approaches to the traditional DL that enable the integration of pre-trained CNN denoisers, such as DnCNN [12] or DRUNet [13], as image priors within iterative algorithms. When equipped with advanced CNN denoisers, PnP/RED provide excellent performance by exploiting both the implicit prior, characterized by a denoiser, and the measurement model [14–22]. *Deep Unfolding (DU)* is a related approach that interprets the iterations of an image recovery algorithm as layers of a neural network and trains it end-to-end in a supervised fashion. Unlike in PnP/RED, the CNN in DU is trained jointly with the measurement model, leading to an image prior optimized for a given inverse problem [23–29]. DU architectures, however, are usually limited to a small number of unfolded iterations due to the high computational and memory complexity of training.

Recent work on *Neural ODEs* [30–32] and *Deep Equilibrium Models (DEQ)* [33–38] has shown the potential benefits of *implicit neural networks* in a number of DL tasks. For example, DEQ was recently used to train CNN priors within PnP/RED iterations by differentiating through the fixed points of the corresponding iterations [35]. Training PnP/RED using DEQ is equivalent to training an infinite depth feedforward network integrating a physical measurement model and CNN prior. However, the training of such networks can still be a significant computational and memory challenge in applications that require processing of a large number

*These authors contributed equally.

of sensor measurements. Specifically, the data-consistency layers in [35] are based on *batch* processing, which means that the *entire set of measurements* is processed at each layer. While this type of batch data processing is known to be suboptimal in traditional large-scale optimization [39–42], the issue has never been considered in the context of training of implicit networks such as those specified via PnP/RED iterations.

This paper addresses this issue by proposing *Online Deep Equilibrium RED (ODER)* as the first DEQ framework for inverse problems that adopts *stochastic processing* of measurements within an implicit neural network. We argue that the proposed *online* approach can improve training and testing efficiency compared to its *batch* counterpart in a number of applications where the number of measurements is large. ODER can be implemented using the fixed-point iterations of RED by introducing stochastic approximations to the corresponding forward and backward DEQ passes. The CNN prior within ODER is trained end-to-end to remove artifacts due to the imaging system and stochastic processing. We present theoretical insights into the convergence of forward and backward passes of ODER, and show its ability to approximate learning using the traditional batch DEQ approach. We show the practical relevance of ODER by solving inverse problems in *intensity diffraction tomography (IDT)* [21, 43], *sparse-view computed tomography (CT)* [44] and accelerated parallel *magnetic resonance imaging (MRI)* [45, 46]. Our numerical results show the ability of ODER to match the imaging quality of the batch DEQ learning at a fraction of complexity. Our work thus addresses an important gap in the current literature on PnP/RED, DU, and DEQ by providing an efficient framework applicable to a wide variety of imaging inverse problems.

All proofs and some technical details that have been omitted for space appear in the appendix, which also provides more background and simulations.

2 Background

Inverse problems. Many imaging problems—such as IDT, CT, and MRI—can be formulated as an inverse problem involving the recovery of an image $\mathbf{x}^* \in \mathbb{R}^n$ from noisy measurements $\mathbf{y} = \mathbf{A}\mathbf{x}^* + \mathbf{e}$, where $\mathbf{A} \in \mathbb{R}^{m \times n}$ is the measurement operator and $\mathbf{e} \in \mathbb{R}^m$ is the noise. A common approach to estimate \mathbf{x}^* is to solve an optimization problem

$$\hat{\mathbf{x}} = \arg \min_{\mathbf{x} \in \mathbb{R}^n} \{g(\mathbf{x}) + h(\mathbf{x})\}, \quad (1)$$

where g is a data-fidelity term that quantifies consistency with the observed data \mathbf{y} and h is a regularizer that encodes prior knowledge on \mathbf{x} . A widely-used data-fidelity term and regularizer in inverse problems are $g(\mathbf{x}) = \frac{1}{2}\|\mathbf{y} - \mathbf{A}\mathbf{x}\|_2^2$ and the *total variation (TV)* function $h(\mathbf{x}) = \tau\|\mathbf{D}\mathbf{x}\|_1$, where \mathbf{D} is the gradient operator and $\tau > 0$ is the regularization parameter [47–49].

PnP, RED, and DU. PnP [10, 15] and RED [11] are two related classes of iterative algorithms that use *additive white Gaussian noise (AWGN)* denoisers, such as BM3D [50] or DnCNN [12], as priors for inverse problems (see the recent review [51]). Since for general denoisers PnP/RED do not solve an optimization problem [18], it is common to interpret PnP/RED as fixed-point iterations of some high-dimensional operators. For example, given a denoiser $\mathbf{D}_\theta : \mathbb{R}^n \rightarrow \mathbb{R}^n$ parameterized by a CNN with weights θ , the *steepest descent* variant of RED (SD-RED) [11] can be written as

$$\mathbf{x}^k = \mathbf{T}_\theta(\mathbf{x}^{k-1}) = \mathbf{x}^{k-1} - \gamma \mathbf{G}_\theta(\mathbf{x}^{k-1}) \quad \text{with} \quad \mathbf{G}_\theta(\mathbf{x}) := \nabla g(\mathbf{x}) + \tau(\mathbf{x} - \mathbf{D}_\theta(\mathbf{x})), \quad (2)$$

where g is the data-fidelity term, and $\gamma, \tau > 0$ are the step size and the regularization parameters, respectively. SD-RED thus seeks to compute a fixed-point $\bar{\mathbf{x}} \in \mathbb{R}^n$ of the operator \mathbf{T}

$$\bar{\mathbf{x}} \in \text{Fix}(\mathbf{T}_\theta) := \{\mathbf{x} \in \mathbb{R}^n : \mathbf{T}_\theta(\mathbf{x}) = \mathbf{x}\} \Leftrightarrow \mathbf{G}_\theta(\bar{\mathbf{x}}) = \nabla g(\bar{\mathbf{x}}) + \tau(\bar{\mathbf{x}} - \mathbf{D}_\theta(\bar{\mathbf{x}})) = \mathbf{0}, \quad (3)$$

The solutions of (3) balance the requirements to be both data-consistent (via ∇g) and noise-free (via $(\mathbf{I} - \mathbf{D}_\theta)$), which can be intuitively interpreted as finding an equilibrium between the physical measurement model and learned prior model. Remarkably, this heuristic of using denoisers not necessarily associated with any h within an iterative algorithm exhibited great empirical success [20, 22, 52–59] and spurred a great deal of theoretical work on PnP/RED [14, 17–19, 60–66]. It is worth mentioning that there has been considerable effort in

reducing the *test-time* computational/memory complexity of PnP/RED by designing online and stochastic PnP/RED algorithms [21, 61, 65, 67].

DU (also known as *algorithm unrolling*) is a DL paradigm that has gained popularity due to its ability to systematically connect iterative algorithms and deep neural network architectures (see reviews in [3, 68]). Many PnP/RED algorithms have been turned into DU architectures by parameterizing the operator D_θ as a CNN with weights θ , truncating the PnP/RED algorithm to a fixed number of iterations, and training the corresponding architecture end-to-end in a supervised fashion. Recent work has explored strategies for reducing the memory and computational complexity of training DU architectures [69, 70]. However, a key bottleneck in DU training is the necessity to store the intermediate activation values required for computing the backpropagation updates, which fundamentally limits the number of unfolding layers one can practically use in large-scale applications.

DEQ. DEQ [33] is a recent method for training infinite-depth, weight-tied feedforward networks by analytically backpropagating through the fixed points using implicit differentiation. The DEQ output is specified implicitly as a fixed point of an operator T_θ parameterized by weights θ

$$\bar{x} = T_\theta(\bar{x}). \quad (4)$$

The DEQ forward pass estimates \bar{x} in (4) by either running a fixed-point iteration or using an optimization algorithm. The DEQ backward pass produces gradients with respect to θ by implicitly differentiating through the fixed points without the knowledge of how they are estimated

$$\ell(\theta) = \frac{1}{2} \|\bar{x}(\theta) - x^*\|_2^2 \Rightarrow \nabla \ell(\theta) = (\nabla_\theta T_\theta(\bar{x}))^\top (I - \nabla_x T_\theta(\bar{x}))^{-\top} (\bar{x} - x^*), \quad (5)$$

where ℓ is the loss function, x^* is the training label, and I is the identity mapping. The vector product with the inverse-Jacobian in (5) can be approximated by solving the following fixed-point equation

$$\bar{b} := (I - \nabla_x T_\theta(\bar{x}))^{-\top} (\bar{x} - x^*) \Rightarrow \bar{b} = (\nabla_x T_\theta(\bar{x}))^\top \bar{b} + (\bar{x} - x^*). \quad (6)$$

Recent work has also explored Jacobian-free DEQ by replacing the inverse-Jacobian with an identity mapping I , leading to a faster training [37].

The comparison of equations (2), (3), and (4) highlights an elegant connection between PnP/RED and DEQ. This connection was explored in the recent work [35] by using DEQ for learning the weights of the CNN prior D_θ end-to-end within PnP/RED iterations. Within the framework of [35], PnP/RED is used for the forward pass and a backward pass is obtained by using (6) on the PnP/RED operators. Specifically, the CNN prior in SD-RED can be trained by running the backward pass using T_θ in (2)

$$b^k = F(b^{k-1}) = (\nabla_x T_\theta(\bar{x}))^\top b^{k-1} + (\bar{x} - x^*). \quad (7)$$

This work makes several new contributions to the existing literature on PnP/RED, DU, and DEQ. The focus is to explore the impact of approximating T_θ in (4) with a “simpler” operator \hat{T}_θ . Following [35], we focus on inverse problems by using PnP/RED operators of form (2) that integrate the physical measurement models and learned CNN priors. We give algorithmic, theoretical, and numerical evidence that one can achieve significant memory/computational gains, while preserving the performance of the original DEQ approach in [35]. It is worth noting that the results here have the potential to generalize to many other implicit neural networks beyond those specified via PnP/RED.

3 Online Deep Equilibrium Method

We consider inverse problems where the data-fidelity term g can be expressed as

$$g(x) = \frac{1}{b} \sum_{i=1}^b g_i(x), \quad (8)$$

where each g_i depends only on the subset $\mathbf{y}_i \in \mathbb{R}^{m_i}$ of the full measurements $\mathbf{y} \in \mathbb{R}^m$ as

$$\mathbb{R}^m = \mathbb{R}^{m_1} \times \mathbb{R}^{m_2} \times \dots \times \mathbb{R}^{m_b} \quad \text{with} \quad m = m_1 + m_2 + \dots + m_b.$$

We are primarily interested in scenarios where the memory/computational complexity of the gradient ∇g is proportional to b . Thus, when $b \rightarrow \infty$, the memory and computational complexity of traditional DEQ to train the CNN prior within the batch PnP/RED algorithms becomes impractical.

To decouple the computational/memory complexity of DEQ from b , we adopt *online* processing of measurements, where g is approximated using a minibatch of $w \ll b$ measurements

$$\hat{g}(\mathbf{x}) = \frac{1}{w} \sum_{s=1}^w g_{i_s}(\mathbf{x}) \quad \Rightarrow \quad \nabla \hat{g}(\mathbf{x}) = \frac{1}{w} \sum_{s=1}^w \nabla g_{i_s}(\mathbf{x}) \quad \Rightarrow \quad \mathbf{H} \hat{g}(\mathbf{x}) = \frac{1}{w} \sum_{s=1}^w \mathbf{H} g_{i_s}(\mathbf{x}), \quad (9)$$

where $\{i_1, \dots, i_w\}$ are i.i.d random variables selected uniformly from the set $\{1, \dots, b\}$. Note that (9) directly implies the *unbiasedness* of the online gradient $\mathbb{E}[\nabla \hat{g}(\mathbf{x})] = \nabla g(\mathbf{x})$ and Hessian $\mathbb{E}[\mathbf{H} \hat{g}(\mathbf{x})] = \mathbf{H} g(\mathbf{x})$ with the expectations taken over the random indices $\{i_1, \dots, i_w\}$.

3.1 Forward Pass

The forward-pass of ODER is performed as follows

$$\mathbf{x}^k = \hat{\mathbf{T}}_{\theta}(\mathbf{x}^{k-1}) = \mathbf{x}^{k-1} - \gamma(\nabla \hat{g}(\mathbf{x}^{k-1}) + \tau \mathbf{R}_{\theta}(\mathbf{x}^{k-1})), \quad k = 1, 2, \dots, K, \quad (10)$$

where $\mathbf{R}_{\theta} = \mathbf{I} - \mathbf{D}_{\theta}$ is the residual of the CNN prior \mathbf{D}_{θ} . The residual \mathbf{R}_{θ} takes artifact-corrupted images at the input and produces the corresponding artifacts at the output. Note how the ODER forward-pass is independent of b since it uses a minibatch approximation $\nabla \hat{g}$ in (9).

It is worth mentioning that when considered separately from DEQ, the forward pass of ODER corresponds to the existing online RED algorithm [21, 71]. The contribution of this work is thus not the forward pass, but the integration of the online forward pass into the DEQ framework via the online backward pass, resulting in a more scalable and flexible DEQ framework for inverse problems.

3.2 Backward Pass

The backward pass of ODER for the MSE loss in (5) is performed as follows

$$\mathbf{b}^k = \hat{\mathbf{F}}(\mathbf{b}^{k-1}) = \left[\nabla_{\mathbf{x}} \hat{\mathbf{T}}_{\theta}(\mathbf{x}^K) \right]^{\top} \mathbf{b}^{k-1} + (\mathbf{x}^K - \mathbf{x}^*), \quad k = 1, 2, \dots, K, \quad (11)$$

starting from $\mathbf{b}^0 = \mathbf{0}$, where \mathbf{x}^K is the final iterate of the forward pass (10) at iteration $K \geq 1$. In both traditional and online backward passes, conventional auto-differentiation tools enable the computation of the Jacobian-vector products in (7) and (11). However, the key difference is that the computational complexity of ODER does not depend on the total number of measurements b .

3.3 ODER Learning

ODER seeks to minimize the MSE loss over $p \geq 1$ training samples

$$\ell(\boldsymbol{\theta}) = \frac{1}{p} \sum_{j=1}^p \ell_j(\boldsymbol{\theta}) \quad \text{with} \quad \ell_j(\boldsymbol{\theta}) = \frac{1}{2} \|\bar{\mathbf{x}}_j(\boldsymbol{\theta}) - \mathbf{x}_j^*\|_2^2, \quad (12)$$

using approximate gradients $\nabla \hat{\ell}_j(\boldsymbol{\theta})$ computed via the online forward and backward passes that are independent of b . Here, $\boldsymbol{\theta}$ denotes the weights of the CNN prior, \mathbf{x}_j^* is the j th training label, and $\bar{\mathbf{x}}_j(\boldsymbol{\theta})$ is the fixed-point of the full-batch SD-RED algorithm (3). The backward pass of ODER can be integrated within any gradient-based optimizer, such as the *stochastic gradient descent (SGD)*. At training iteration $t \geq 1$ we generate

two sets of independent random variables. First, the index j_t is selected uniformly at random from $\{1, \dots, p\}$, then online forward and backward passes are computed using the measurement models in (9). We can thus express the SGD update rule as follows

$$\boldsymbol{\theta}^{t+1} = \boldsymbol{\theta}^t - \beta \nabla \hat{\ell}_{j_t}(\boldsymbol{\theta}^t) \quad \text{with} \quad \nabla \hat{\ell}_{j_t}(\boldsymbol{\theta}^t) = \left[\nabla_{\boldsymbol{\theta}} \hat{\mathbb{T}}_{\boldsymbol{\theta}^t}(\mathbf{x}_{j_t}^K) \right]^\top \mathbf{b}_{j_t}^K, \quad (13)$$

where $\beta > 0$ is the SGD learning rate, $\mathbf{x}_{j_t}^K$ and $\mathbf{b}_{j_t}^K$ are the final iterates of the ODER forward and backward passes at the training index j_t after $K \geq 1$ iterations.

4 Theoretical Analysis

Our theoretical analysis relies on a set of explicit assumptions serving as sufficient conditions. The proofs of all the theorems will be provided in the supplement.

Assumption 1. Each g_i is twice continuously differentiable and convex. There exists $\lambda > 0$ such that each gradient ∇g_i and Hessian $\text{H}g_i$ are λ -Lipschitz continuous.

The fact that g is twice continuously differentiable is needed for the backward pass. The assumption that all the Lipschitz constants are the same is only needed to streamline mathematical exposition.

Assumption 2. $D_{\boldsymbol{\theta}}(\mathbf{x})$ is continuously differentiable with respect to $\boldsymbol{\theta}$ and \mathbf{x} . There exists $\alpha > 0$ such that $D_{\boldsymbol{\theta}}(\mathbf{x})$, $\nabla_{\mathbf{x}} D_{\boldsymbol{\theta}}(\mathbf{x})$, and $\nabla_{\boldsymbol{\theta}} D_{\boldsymbol{\theta}}(\mathbf{x})$ are α -Lipschitz continuous with respect to $\boldsymbol{\theta}$ and \mathbf{x} . Finally, we also assume that $D_{\boldsymbol{\theta}}$ is a contraction, which means that there exists $\kappa < 1$ such that

$$\|D_{\boldsymbol{\theta}}(\mathbf{z}) - D_{\boldsymbol{\theta}}(\mathbf{y})\|_2 \leq \kappa \|\mathbf{z} - \mathbf{y}\|_2, \quad \forall \mathbf{z}, \mathbf{y} \in \mathbb{R}^n.$$

Since $D_{\boldsymbol{\theta}}$ is a CNN, its differentiability is a standard assumption. The contractive $D_{\boldsymbol{\theta}}$ and convex g , ensure that $\mathbb{T}_{\boldsymbol{\theta}}$ is a contraction, enabling provable convergence of the forward and backward passes. The design of contractive $\mathbb{T}_{\boldsymbol{\theta}}$ is a common PnP/RED strategy to ensure convergence [19, 35, 65].

Assumption 3. There exists $R > 0$ such that for all $\bar{\mathbf{x}} \in \text{Fix}(\mathbb{T})$ and $\bar{\mathbf{b}} \in \text{Fix}(\mathbb{F})$, we have $\|\mathbf{x}^k - \bar{\mathbf{x}}\|_2 \leq R$ and $\|\mathbf{b}^k - \bar{\mathbf{b}}\|_2 \leq R$ for all $k \in \{1, \dots, K\}$.

The existence of the bound R is reasonable, as many images have bounded pixel values. Similarly, the bound on \mathbf{b}^k is also reasonable for ensuring bounded DEQ gradients.

Assumption 4. There exists $\nu > 0$ such that for all $\mathbf{x} \in \mathbb{R}^n$, we have

$$\mathbb{E} [\|\nabla g(\mathbf{x}) - \nabla \hat{g}(\mathbf{x})\|_2^2] \leq \frac{\nu^2}{w} \quad \text{and} \quad \mathbb{E} [\|\text{H}g(\mathbf{x}) - \text{H}\hat{g}(\mathbf{x})\|_2^2] \leq \frac{\nu^2}{w},$$

where the expectations are taken over $\{i_1, \dots, i_w\}$.

The variance bounds are standard in stochastic algorithms. The variance bounds on the gradient and Hessian approximations are thus reasonable in this context. The decrease of the bounds for higher values of w is natural since \hat{g} is an unbiased estimator of g obtained averaging w independent terms.

Theorem 1. Run the forward pass of ODER for $k \geq 1$ iterations under Assumptions 1-4 using the step size $0 < \gamma < 1/(\lambda + \tau)$. Then, the sequence of forward pass iterates satisfies

$$\mathbb{E} [\|\mathbf{x}^k - \bar{\mathbf{x}}\|_2] \leq \eta^k R + \frac{\gamma \nu}{(1 - \eta)\sqrt{w}}, \quad (14)$$

for some constant $0 < \eta < 1$ where $\bar{\mathbf{x}} \in \text{Fix}(\mathbb{T})$.

Theorem 1 is a variation on the convergence results for online RED/PnP [21, 61, 65, 67], showing that the forward pass converges to $\bar{\mathbf{x}} \in \text{Fix}(\mathbb{T})$ up to an error term that can be controlled via γ and w .

Theorem 2. *Run the backward pass of ODER for $k \geq 1$ iterations under Assumptions 1-4 from $\mathbf{b}^0 = \mathbf{0}$ using the step-size $0 < \gamma < 1/(\lambda + \tau)$. Then, the sequence of backward pass iterates satisfies*

$$\mathbb{E} [\|\mathbf{b}^k - \bar{\mathbf{b}}\|_2] \leq B_1 \eta^k + \frac{B_2}{\sqrt{w}}, \quad (15)$$

where $0 < \eta < 1$, $B_1 > 0$ and $B_2 > 0$ are constants independent of k and w , and $\bar{\mathbf{b}} \in \text{Fix}(\mathbb{F})$.

Theorem 2 shows that the online backward pass in expectation converges to $\bar{\mathbf{b}}$ up to an error term that can be controlled via w . The complete expressions for constants B_1 and B_2 are in the proof.

Assumption 5. *Function ℓ has a global minimizer $\boldsymbol{\theta}^*$ and has a L -Lipschitz continuous gradient, which means that for all $\boldsymbol{\theta}, \phi$, we have $\|\nabla \ell(\boldsymbol{\theta}) - \nabla \ell(\phi)\|_2 \leq L\|\boldsymbol{\theta} - \phi\|_2$.*

Assumption 6. *The loss function in (12) and indices $\{j_t\}$ in (13) are such that*

$$\mathbb{E} [\nabla \ell_{j_t}(\boldsymbol{\theta})] = \nabla \ell(\boldsymbol{\theta}) \quad \text{and} \quad \mathbb{E} [\|\nabla \ell_{j_t}(\boldsymbol{\theta}) - \nabla \ell(\boldsymbol{\theta})\|_2^2] \leq \sigma^2,$$

where the expectations are taken with respect to the random index uniformly as $j_t \in \{1, \dots, p\}$.

The existence of a minimizer and the Lipschitz continuity of the loss gradient are standard assumptions in the literature [42, 72, 73]. Note that we do *not* assume that the training loss ℓ is convex. Assumption 6 is the standard assumption used in the analysis of SGD.

Theorem 3. *Train ODER using SGD for $T \geq 1$ iterations under Assumptions 1-6 using the step-size parameters $0 < \beta \leq 1/L$ and the minibatch size $w \geq 1$. Select a large enough number of forward and backward pass iterations $K \geq 1$ to satisfy $0 < \eta^K \leq 1/\sqrt{w}$. Then, we have that*

$$\frac{1}{T} \sum_{t=0}^{T-1} \mathbb{E} [\|\nabla \ell(\boldsymbol{\theta}^t)\|_2^2] \leq \frac{2(\ell(\boldsymbol{\theta}^0) - \ell(\boldsymbol{\theta}^*))}{\beta T} + \frac{C_1}{\sqrt{w}} + \beta C_2.$$

where $C_1 > 0$ and $C_2 > 0$ are constants independent of T and w .

The complete expressions for constants C_1 and C_2 are in the proof. Theorem 3 allows us to understand the ability of the iterates generated using (13) to approximate the stationary points of the desired loss (12). The error terms in the bound depend on the training step-size β and the minibatch size w , both of which can be controlled during training. In summary, we presented several theoretical results that give insights into ODER by stating explicit sufficient conditions and approximation bounds.

5 Numerical Evaluation

We numerically validate ODER in the context of three computational imaging modalities: IDT, sparse-view CT, and parallel MRI. Our goal is to both (a) empirically evaluate the performance of ODER and (b) highlight its effectiveness for processing a large number of measurements. We adopt ℓ_2 -norm loss $g(\mathbf{x}) = \frac{1}{2}\|\mathbf{y} - \mathbf{A}\mathbf{x}\|_2^2$ as the data-fidelity term for all three imaging modalities.

ODER is compatible with any CNN architecture used to implement \mathbb{D}_θ . We use a *tiny* U-Net architecture [70] for ODER and the traditional RED (DEQ) [35]. We have added spectral normalization [74] to all the layers of CNN for stability (see the supplement for the numerical evaluation of the contractiveness of \mathbb{T}_θ on all three modalities). Similar to [35], the CNN prior of ODER and RED (DEQ) are initialized using pre-trained denoisers. During the training of both ODER and RED (DEQ), we use the *Nesterov acceleration* [72] for the forward pass and *Anderson acceleration* [75] for the backward pass. We also adopt the stopping criterion

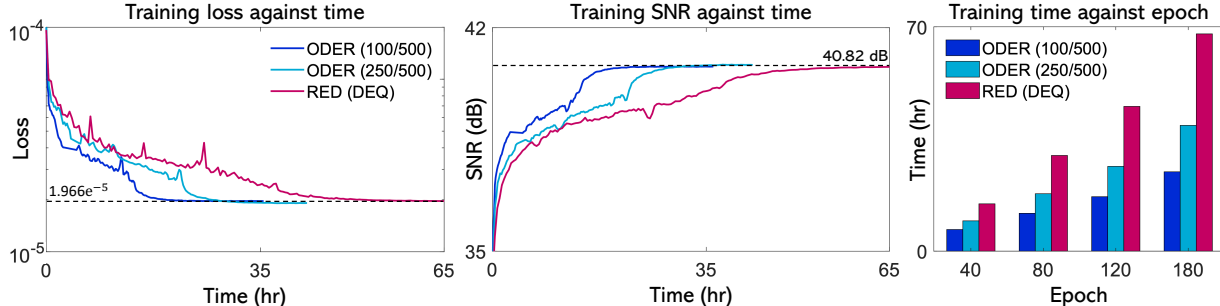


Figure 1: Quantitative evaluation of ODER on IDT for two minibatch sizes $w \in \{100, 250\}$ used at each step of the network against RED (DEQ) using the full batch of $b = 500$ measurements. The left figure plots the loss against time in hours for different values of w evaluated on the training set. The middle and right figures plot the corresponding SNR against time and the amount of time required to reach a certain epoch for different values of w . By using minibatches $1 \leq w \leq b$, ODER can achieve nearly $2.5\times$ improvement in training time over RED (DEQ) for a similar final imaging quality.

Table 1: IDT image recovery for different input SNR (dB) values on images from [77]. We also present model size and per-iteration memory usage for the measurements, and average test-times.

Method	Input SNR (dB)			Size		Time	
	15	20	25	Model	Meas.	CPU	GPU
TV	38.34	38.77	38.85	—	3.56 GB	215.3s	32.24s
U-Net	38.35	38.89	39.02	118.2 MB	—	2.811s	0.089s
ISTA-Net+	38.37	38.94	39.27	1.21 MB	3.56 GB	7.081s	0.216s
SGD-Net (100)	39.62	40.26	40.47	29.7 MB	0.71GB	6.697s	0.207s
RED (Denoising)	39.52	40.04	40.41	118.2 MB	3.56 GB	285.5s	7.528s
ODER (100)	40.28	41.42	41.94	29.7 MB	0.71 GB	63.31s	2.051s
ODER (250)	40.57	41.50	41.96	29.7 MB	1.76 GB	118.7s	3.628s
RED (DEQ)	40.54	41.51	41.95	29.7 MB	3.56 GB	202.3s	6.362s

from [35, 76] by setting residual tolerance to 10^{-3} for both forward and backward iterations (see supplement for additional details).

For reference we include several other well-known baseline methods, including TV [47], U-Net [4] and ISTA-Net⁺ [23]. We also include the unfolded RED (Unfold) [70] and the traditional RED (Denoising) [11] to illustrate the improvements due to DEQ. TV is an iterative method that does not require training, while other methods are all DL-based with publicly available implementations. We use the U-Net architecture in [4] as the AWGN denoiser for RED, while we use the same tiny U-Net for RED (Unfold) as in RED (DEQ). For each imaging modality, we trained the denoiser in RED (Denoising) for AWGN removal at five noise levels corresponding to $\sigma \in \{2, 7, 5, 10, 15\}$. For each experiment, we select the denoiser achieving the highest SNR. In all the experiments, we train ODER and RED (DEQ) using the same training strategy and parameter initialization settings. We use `fminbound` in the `scipy.optimize` toolbox to identify the optimal regularization parameters for TV, RED (Denoising), ODER and RED (DEQ) at the inference time.

5.1 Image Reconstruction in IDT

IDT [43] is a data intensive computational imaging modality that seeks to recover the spatial distribution of the complex-valued permittivity contrast of an object given a set of its intensity-only measurements. Specifically, \mathbf{A} consists of a set of b complex measurement operators $[\mathbf{A}_1, \dots, \mathbf{A}_b]^T$, where each \mathbf{A}_i is a convolution corresponding to the i th measurement \mathbf{y}_i . In the simulation, we randomly extracted and cropped 400 slices of

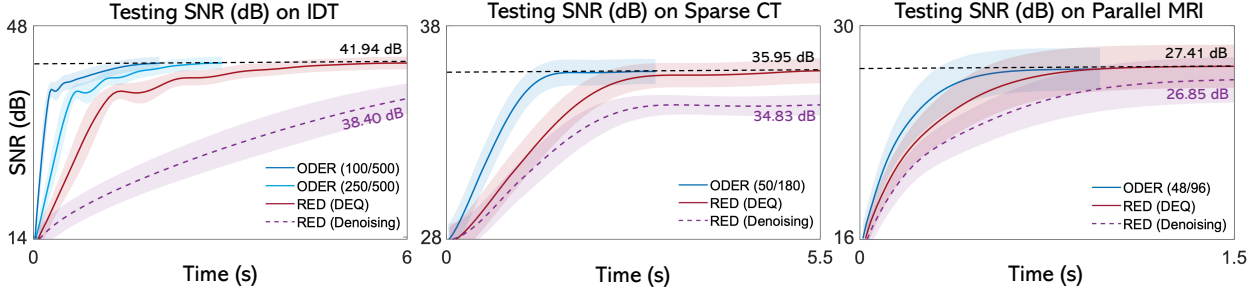


Figure 2: Illustration of the convergence speed of ODER, RED (DEQ) and RED (Denoising) for three imaging applications. **Left:** IDT with the full batch of $b = 500$ measurements under 25 dB input SNR. **Middle:** Sparse-view CT with $b = 180$ projection views. **Right:** Parallel MRI at 20% sampling with $b = 96$ simulated coil sensitivity maps. ODER achieves $1.4 \times \sim 3 \times$ speedup over RED (DEQ) at inference time without significant degradation in accuracy across three problems.

Table 2: Sparse-view CT image recovery in terms of SNR (dB) and SSIM on test images from [78]. The last two columns provide the average test-times for a 512×512 image using 180 views.

Method	Projection Views						Time	
	90		120		180		CPU	GPU
TV	29.44	0.9688	30.27	0.9731	31.33	0.9771	768.1s	15.61s
U-Net	33.05	0.9741	34.02	0.9790	35.11	0.9815	4.014s	0.056s
ISTA-Net+	32.15	0.9706	33.38	0.9755	34.83	0.9812	37.38s	0.344s
RED (Unfold)	33.97	0.9753	35.01	0.9824	35.78	0.9835	29.93s	0.256s
RED (Denoising)	32.64	0.9708	33.60	0.9789	34.83	0.9807	498.5s	5.549s
ODER	34.40	0.9824	35.12	0.9841	35.91	0.9859	334.1s	3.113s
RED (DEQ)	34.61	0.9826	35.26	0.9845	35.95	0.9861	616.1s	5.466s

416×416 images for training, 28 images for validation and 56 images for testing from Brecahad database [77]. Following the setup in [21, 43], we generated $b = 500$ intensity measurements under AWGN corresponding to $\{15, 20, 25\}$ dB of input SNR. ODER and RED (DEQ) were trained at the noise level corresponding to 20 dB input SNR. In our comparisons, we also included the recent SGD-Net [70] method that corresponds to RED (Unfold), but uses stochastic data-consistency layers similar to ODER. SGD-Net allows for more unfolded iteration blocks by improving the usage of limited GPU memory. Both ODER and RED (DEQ) were trained using SGD, while all other methods were trained using Adam [79].

Fig. 5 compares the average loss and SNR achieved by RED (DEQ) with ($b = 500$) and ODER with $w \in \{100, 250\}$ during training. It took 67.49 hours to train RED (DEQ) for 180 epochs. It took 24.76 and 39.23 hours to train ODER with ($w = 100$) and ($w = 250$), respectively, for the same number epochs. Table 5 provides the final SNR achieved by ODER and several baseline methods on the test data. The runtime in the table corresponds to the average inference time that excludes the model loading. ODER with ($w = 100$) is around $3 \times$ faster than RED (DEQ) on both GPU and CPU. Fig. 2 (left) highlights the faster convergence of ODER compared to RED (DEQ) to the similar SNR.

ODER is memory efficient due to its online processing of measurements. The memory considerations in IDT include the size of all the variables related to the desired image x , the measured data y_i , and the variables related to the measurement operator $\{A_i\}$. ODER addresses the problem of storing and processing the measurements and the measurement operators on the GPU during end-to-end training. Table 5 shows the total memory (GB) used by ODER and RED (DEQ) for reconstructing a 416×416 pixel permittivity image. While RED (DEQ) requires 3.56 GB of GPU memory in every iteration, ODER with $w = 100$ requires only 0.71 GB, which is about 20% of the full volume.

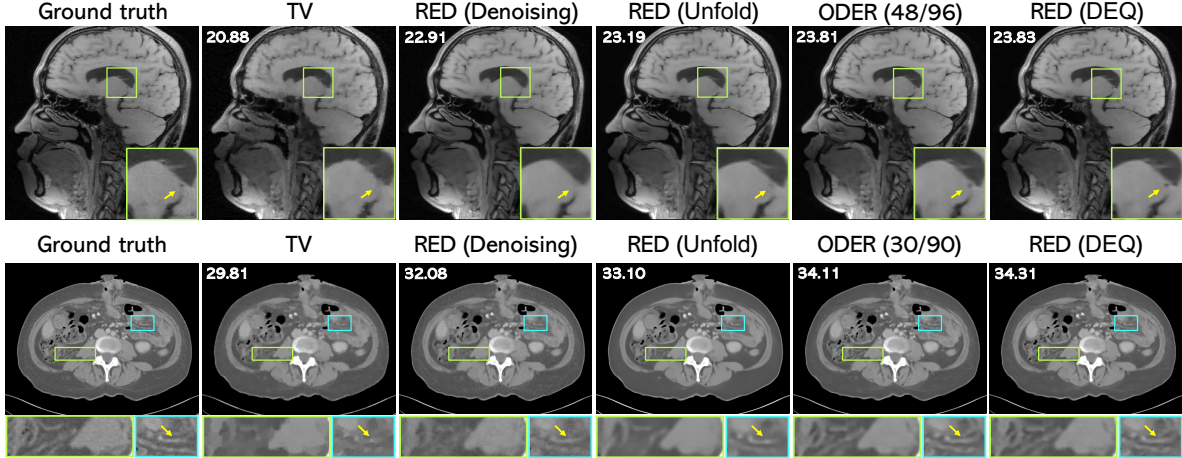


Figure 3: Visual evaluation of several well-known methods on two imaging problems: (top) Reconstruction of a brain image from its radial Fourier measurements at 10% sampling with $b = 96$ simulated coil sensitivity maps; (bottom) Reconstruction of a body CT image from $b = 90$ projection views. Note the similar performance of ODER and RED (DEQ), and the improvement over RED (Denoising) /RED (Unfold) due to the usage of DEQ learning. Best viewed by zooming in the display.

Table 3: Average SNR (dB), SSIM, and running times for several methods on MRI images. The last two columns provide the average test-times for a 320×320 image using 96 simulated coils.

Method	MRI Set1 [23]				MRI Set2 [83]		Time	
	10%	SSIM	20%	SSIM	10%	SSIM	CPU	GPU
TV	20.88	0.9059	24.87	0.9445	24.84	0.9674	122.2s	7.591s
U-Net	23.07	0.9329	26.42	0.9562	26.04	0.9712	0.683s	0.011s
ISTA-Net+	22.95	0.9298	26.31	0.9546	25.82	0.9693	8.993s	0.264s
RED (Unfold)	23.37	0.9363	26.81	0.9591	26.37	0.9744	8.744s	0.231s
RED (Denoising)	23.29	0.9352	26.85	0.9598	26.42	0.9748	272.4s	7.511s
ODER	24.08	0.9442	27.22	0.9649	27.03	0.9783	120.0s	3.005s
RED (DEQ)	24.10	0.9451	27.41	0.9660	27.10	0.9789	166.9s	4.577s

5.2 Image Reconstruction in Sparse-View CT

We consider simulated data obtained from the clinically realistic CT images provided by Mayo Clinic for the *low dose CT grand challenge* [78]. Specifically, 2070 2D slices of size 512×512 corresponding to 7 patients were used to train the models. The test images correspond to 55 slices randomly selected from another patient. We implement the measurement operator A and its adjoint A^T with PyTorch implementation of Radon and IRadon¹ transform. We assume that the CT machine is designed to project from nominal angles with $b \in \{90, 120, 180\}$ projection views that are evenly-distributed on a half circle and 724 detector pixels. We add Gaussian noise to the sinograms to make the input SNR equal to 50 dB. We empirically found that using Adam [79] is around $2\times$ faster than applying SGD when training both ODER and RED (DEQ). We thus trained all learning-based methods using Adam. Table 4 reports the average SNR and SSIM results for ODER with (w/b) of $\{30/90, 40/120, 50/180\}$ and all baselines. Fig. 2 (middle) reports the convergence speed of ODER with $(w = 50)$ for sparse-view CT with full batch ($b = 180$) views. The visual comparisons are in Fig. 3 (bottom). Note how ODER matches the performance of RED (DEQ) and outperforms RED (Denoising) and RED (Unfold) across different projection views.

¹The code is publicly available at https://github.com/phernst/pytorch_radon

5.3 Image Reconstruction in Accelerated Parallel MRI

We simulated a multi-coil CS-MRI setup using radial Fourier sampling [80, 81]. The measurement operator \mathbf{A} thus consists of a set of b complex measurement operators depending on a set of receiver coils $\{\mathbf{S}_i\}$ [82]. For each coil, we have $\mathbf{A}_i = \mathbf{P}\mathbf{F}\mathbf{S}_i$, where \mathbf{P} is the diagonal sampling matrix, \mathbf{F} is the Fourier transform, and \mathbf{S}_i is the diagonal matrix of sensitivity maps. ODER is evaluated on two brain MRI datasets. The first dataset [23] provides 800 slices of 256×256 images for training and 50 slices for testing. The second dataset [83] contains a randomly selected 400 volumes of $320 \times 320 \times 10$ images for training, and 32 volumes for testing. We synthesized the total number of ($b = 96$) 2D/3D coil sensitivity maps using the SigPy [84] for each dataset, respectively. Since all the CNNs in our numerical study are 2D, we apply them slice-by-slice when forming 3D volumes (all slices are passed in parallel using batch processing). We trained all learning-based methods using Adam. Fig. 2 (right) reports the convergence speed of ODER for CS-MRI at 20% sampling. Table 3 reports the average SNR and SSIM values for ODER with ($w = 48$) and all baseline methods. The visual comparison can be found in Fig. 3 (top) at 10% sampling.

6 Conclusion and Future Work

This work proposes ODER as a new online DEQ learning method for RED, analyzes its theoretical properties in terms of convergence and accuracy, and applies it to three widely-used imaging inverse problems. ODER extends the recent DEQ approach in [35] by introducing randomized processing of measurements. Our extensive theoretical and numerical results corroborate the potential of ODER to reduce the computational/memory complexity of training and testing, while achieving similar imaging quality as RED (DEQ). The future work can explore to further improve our analysis and design distributed variants of ODER to enhance its performance on parallel computing architectures.

Acknowledgements

Research presented in this article was supported by the NSF CAREER award CCF-2043134.

References

- [1] M. T. McCann, K. H. Jin, and M. Unser, “Convolutional neural networks for inverse problems in imaging: A review,” *IEEE Signal Process. Mag.*, vol. 34, no. 6, pp. 85–95, 2017.
- [2] A. Lucas, M. Iliadis, R. Molina, and A. K. Katsaggelos, “Using deep neural networks for inverse problems in imaging: Beyond analytical methods,” *IEEE Signal Process. Mag.*, vol. 35, no. 1, pp. 20–36, Jan. 2018.
- [3] G. Ongie, A. Jalal, C. A. Metzler, R. G. Baraniuk, A. G. Dimakis, and R. Willett, “Deep learning techniques for inverse problems in imaging,” *IEEE J. Sel. Areas Inf. Theory*, vol. 1, no. 1, pp. 39–56, May 2020.
- [4] O. Ronneberger, P. Fischer, and T. Brox, “U-Net: Convolutional networks for biomedical image segmentation,” in *Proc. Med. Image. Comput. Comput. Assist. Intervent.*, 2015, pp. 234–241.
- [5] K. H. Jin, M. T. McCann, E. Froustey, and M. Unser, “Deep convolutional neural network for inverse problems in imaging,” *IEEE Trans. Image Process.*, vol. 26, no. 9, pp. 4509–4522, Sep. 2017.
- [6] Eunhee Kang, Junhong Min, and Jong Chul Ye, “A deep convolutional neural network using directional wavelets for low-dose x-ray CT reconstruction,” *Medical Physics*, vol. 44, no. 10, pp. e360–e375, 2017.
- [7] H. Chen, Y. Zhang, M. K. Kalra, F. Lin, Y. Chen, P. Liao, J. Zhou, and G. Wang, “Low-dose CT with a residual encoder-decoder convolutional neural network,” *IEEE Trans. Med. Imag.*, vol. 36, no. 12, pp. 2524–2535, Dec. 2017.

- [8] Y. Sun, Z. Xia, and U. S. Kamilov, “Efficient and accurate inversion of multiple scattering with deep learning,” *Opt. Express*, vol. 26, no. 11, pp. 14678–14688, May 2018.
- [9] Y. Han and J. C. Ye, “Framing U-Net via deep convolutional framelets: Application to sparse-view CT,” *IEEE Trans. Med. Imag.*, vol. 37, no. 6, pp. 1418–1429, 2018.
- [10] S. V. Venkatakrisnan, C. A. Bouman, and B. Wohlberg, “Plug-and-play priors for model based reconstruction,” in *Proc. IEEE Global Conf. Signal Process. and Inf. Process.*, Austin, TX, USA, Dec. 3-5, 2013, pp. 945–948.
- [11] Y. Romano, M. Elad, and P. Milanfar, “The little engine that could: Regularization by denoising (RED),” *SIAM J. Imaging Sci.*, vol. 10, no. 4, pp. 1804–1844, 2017.
- [12] K. Zhang, W. Zuo, Y. Chen, D. Meng, and L. Zhang, “Beyond a Gaussian denoiser: Residual learning of deep CNN for image denoising,” *IEEE Trans. Image Process.*, vol. 26, no. 7, pp. 3142–3155, Jul. 2017.
- [13] K. Zhang, Y. Li, W. Zuo, L. Zhang, L. Van Gool, and R. Timofte, “Plug-and-play image restoration with deep denoiser prior,” *IEEE Trans. Patt. Anal. and Machine Intell.*, pp. 1–1, 2021.
- [14] S. H. Chan, X. Wang, and O. A. Elgendy, “Plug-and-play ADMM for image restoration: Fixed-point convergence and applications,” *IEEE Trans. Comp. Imag.*, vol. 3, no. 1, pp. 84–98, Mar. 2017.
- [15] S. Sreehari, S. V. Venkatakrisnan, B. Wohlberg, G. T. Buzzard, L. F. Drummy, J. P. Simmons, and C. A. Bouman, “Plug-and-play priors for bright field electron tomography and sparse interpolation,” *IEEE Trans. Comput. Imaging*, vol. 2, no. 4, pp. 408–423, Dec. 2016.
- [16] U. S. Kamilov, H. Mansour, and B. Wohlberg, “A plug-and-play priors approach for solving nonlinear imaging inverse problems,” *IEEE Signal. Proc. Let.*, vol. 24, no. 12, pp. 1872–1876, Dec. 2017.
- [17] G. T. Buzzard, S. H. Chan, S. Sreehari, and C. A. Bouman, “Plug-and-play unplugged: Optimization free reconstruction using consensus equilibrium,” *SIAM J. Imaging Sci.*, vol. 11, no. 3, pp. 2001–2020, Sep. 2018.
- [18] E. T. Reehorst and P. Schniter, “Regularization by denoising: Clarifications and new interpretations,” *IEEE Trans. Comput. Imag.*, vol. 5, no. 1, pp. 52–67, Mar. 2019.
- [19] Ernest K. Ryu, J. Liu, S. Wang, X. Chen, Z. Wang, and W. Yin, “Plug-and-play methods provably converge with properly trained denoisers,” in *Proc. 36th Int. Conf. Mach. Learn.*, Long Beach, CA, USA, Jun. 09–15 2019, vol. 97, pp. 5546–5557.
- [20] Gary Mataev, Peyman Milanfar, and Michael Elad, “DeepRED: Deep image prior powered by RED,” in *Proc. IEEE Int. Conf. Comput. Vis. Workshops*, Oct. 2019, pp. 1–10.
- [21] Z. Wu, Y. Sun, A. Matlock, J. Liu, L. Tian, and U. S. Kamilov, “SIMBA: Scalable inversion in optical tomography using deep denoising priors,” *IEEE J. Sel. Topics Signal Process.*, vol. 14, no. 6, pp. 1163–1175, Oct. 2020.
- [22] J. Liu, Y. Sun, C. Eldeniz, W. Gan, H. An, and U. S. Kamilov, “RARE: Image reconstruction using deep priors learned without ground truth,” *IEEE J. Sel. Topics Signal Process.*, vol. 14, no. 6, pp. 1088–1099, Oct. 2020.
- [23] J. Zhang and B. Ghanem, “ISTA-Net: Interpretable optimization-inspired deep network for image compressive sensing,” in *Proc. IEEE Conf. Comput. Vision Pattern Recognit.*, 2018, pp. 1828–1837.
- [24] A. Hauptmann, F. Lucka, M. Betcke, N. Huynh, J. Adler, B. Cox, P. Beard, S. Ourselin, and S. Arridge, “Model-based learning for accelerated, limited-view 3-d photoacoustic tomography,” *IEEE Trans. Med. Imag.*, vol. 37, no. 6, pp. 1382–1393, 2018.

- [25] J. Adler and O. Öktem, “Learned primal-dual reconstruction,” *IEEE Trans. Med. Imag.*, vol. 37, no. 6, pp. 1322–1332, June 2018.
- [26] H. K. Aggarwal, M. P. Mani, and M. Jacob, “Modl: Model-based deep learning architecture for inverse problems,” *IEEE Trans. Med. Imag.*, vol. 38, no. 2, pp. 394–405, Feb. 2019.
- [27] S. A. Hosseini, B. Yaman, S. Moeller, M. Hong, and M. Akcakaya, “Dense recurrent neural networks for accelerated MRI: History-cognizant unrolling of optimization algorithms,” *IEEE J. Sel. Topics Signal Process.*, vol. 14, no. 6, pp. 1280–1291, Oct. 2020.
- [28] B. Yaman, S. A. H. Hosseini, S. Moeller, J. Ellermann, K. Uğurbil, and M. Akçakaya, “Self-supervised learning of physics-guided reconstruction neural networks without fully sampled reference data,” *Magn. Reson. Med.*, vol. 84, no. 6, pp. 3172–3191, Jul. 2020.
- [29] S. Mukherjee, M. Carioni, O. Öktem, and C. B. Schönlieb, “End-to-end reconstruction meets data-driven regularization for inverse problems,” in *Advances in Neural Information Processing Systems*, A. Beygelzimer, Y. Dauphin, P. Liang, and J. Wortman Vaughan, Eds., 2021.
- [30] R. T. Q. Chen, Y. Rubanova, J. Bettencourt, and D. K. Duvenaud, “Neural ordinary differential equations,” in *Advances in Neural Information Processing Systems*, S. Bengio, H. Wallach, H. Larochelle, K. Grauman, N. Cesa-Bianchi, and R. Garnett, Eds. 2018, vol. 31, Curran Associates, Inc.
- [31] E. Dupont, A. Doucet, and Y. W. Teh, “Augmented neural odes,” in *Advances in Neural Information Processing Systems*, 2019, vol. 32.
- [32] J. Kelly, J. Bettencourt, M. J. Johnson, and D. K. Duvenaud, “Learning differential equations that are easy to solve,” in *Advances in Neural Information Processing Systems*, H. Larochelle, M. Ranzato, R. Hadsell, M.F. Balcan, and H. Lin, Eds. 2020, vol. 33, pp. 4370–4380, Curran Associates, Inc.
- [33] S. Bai, J. Z. Kolter, and V. Koltun, “Deep equilibrium models,” *Proc. Advances in Neural Information Processing Systems 33*, vol. 32, 2019.
- [34] E. Winston and J. Z. Kolter, “Monotone operator equilibrium networks,” in *Advances in Neural Information Processing Systems*, H. Larochelle, M. Ranzato, R. Hadsell, M.F. Balcan, and H. Lin, Eds. 2020, vol. 33, pp. 10718–10728, Curran Associates, Inc.
- [35] D. Gilton, G. Ongie, and R. Willett, “Deep equilibrium architectures for inverse problems in imaging,” *IEEE Trans. Comput. Imag.*, vol. 7, pp. 1123–1133, 2021.
- [36] K. Kawaguchi, “On the theory of implicit deep learning: Global convergence with implicit layers,” in *International Conference on Learning Representations*, 2021.
- [37] S. W. Fung, H. Heaton, Q. Li, D. McKenzie, S. Osher, and W. Yin, “Jfb: Jacobian-free backpropagation for implicit networks,” *arXiv preprint arXiv:2103.12803*, 2021.
- [38] S. Gurumurthy, S. Bai, Z. Manchester, and J. Z. Kolter, “Joint inference and input optimization in equilibrium networks,” in *Advances in Neural Information Processing Systems*, M. Ranzato, A. Beygelzimer, Y. Dauphin, P.S. Liang, and J. Wortman Vaughan, Eds. 2021, vol. 34, pp. 16818–16832, Curran Associates, Inc.
- [39] L. Bottou and O. Bousquet, “The tradeoffs of large scale learning,” in *Proc. Advances Neural Inf. Process. Syst.*, Vancouver, BC, Canada, Dec. 3-6, 2007, pp. 161–168.
- [40] D. P. Bertsekas, “Incremental proximal methods for large scale convex optimization,” *Math. Program. Ser. B*, vol. 129, pp. 163–195, 2011.

- [41] D. Kim, D. Pal, J. Thibault, and J. A. Fessler, “Accelerating ordered subsets image reconstruction for X-ray CT using spatially nonuniform optimization transfer,” *IEEE Trans. Med. Imag.*, vol. 32, no. 11, pp. 1965–1978, Nov. 2013.
- [42] L. Bottou, F. E. Curtis, and J. Nocedal, “Optimization methods for large-scale machine learning,” *SIAM Rev.*, vol. 60, no. 2, pp. 223–311, 2018.
- [43] R. Ling, W. Tahir, H.-Y. Lin, H. Lee, and L. Tian, “High-throughput intensity diffraction tomography with a computational microscope,” *Biomed. Opt. Express*, vol. 9, no. 5, pp. 2130–2141, May 2018.
- [44] A. C. Kak and M. Slaney, *Principles of Computerized Tomographic Imaging*, IEEE, 1988.
- [45] M A Griswold, P M Jakob, R M Heidemann, M Nittka, V Jellus, J Wang, B Kiefer, and A Haase, “Generalized autocalibrating partially parallel acquisitions (grappa),” *Magn. Reson. in Med.*, vol. 47, no. 6, pp. 1202–1210, 2002.
- [46] M. Uecker, P. Lai, M. J. Murphy, P. Virtue, M. Elad, J. M. Pauly, S. S. Vasanawala, and M. Lustig, “Espirit—an eigenvalue approach to autocalibrating parallel mri: where sense meets grappa,” *Magnetic resonance in medicine*, vol. 71, no. 3, pp. 990–1001, 2014.
- [47] L. I. Rudin, S. Osher, and E. Fatemi, “Nonlinear total variation based noise removal algorithms,” *Physica D*, vol. 60, no. 1–4, pp. 259–268, Nov. 1992.
- [48] J. M. Bioucas-Dias and M. A. T. Figueiredo, “A new TwIST: Two-step iterative shrinkage/thresholding algorithms for image restoration,” *IEEE Trans. Image Process.*, vol. 16, no. 12, pp. 2992–3004, December 2007.
- [49] A. Beck and M. Teboulle, “Fast gradient-based algorithm for constrained total variation image denoising and deblurring problems,” *IEEE Trans. Image Process.*, vol. 18, no. 11, pp. 2419–2434, November 2009.
- [50] K. Dabov, A. Foi, V. Katkovnik, and K. Egiazarian, “Image denoising by sparse 3-D transform-domain collaborative filtering,” *IEEE Trans. Image Process.*, vol. 16, no. 16, pp. 2080–2095, Aug. 2007.
- [51] U. S. Kamilov, C. A. Bouman, G. T. Buzzard, and B. Wohlberg, “Plug-and-play methods for integrating physical and learned models in computational imaging,” 2022, arXiv:2203.17061.
- [52] K. Zhang, W. Zuo, S. Gu, and L. Zhang, “Learning deep CNN denoiser prior for image restoration,” in *Proc. IEEE Conf. Computer Vision and Pattern Recognition (CVPR)*, Honolulu, USA, July 21-26, 2017, pp. 3929–3938.
- [53] C. Metzler, P. Schniter, A. Veeraraghavan, and R. Baraniuk, “prDeep: Robust phase retrieval with a flexible deep network,” in *Proc. 36th Int. Conf. Mach. Learn.*, Stockholm, Sweden, Jul. 10–15 2018, pp. 3501–3510.
- [54] W. Dong, P. Wang, W. Yin, G. Shi, F. Wu, and X. Lu, “Denoising prior driven deep neural network for image restoration,” *IEEE Trans. Pattern Anal. Mach. Intell.*, vol. 41, no. 10, pp. 2305–2318, Oct 2019.
- [55] K. Zhang, W. Zuo, and L. Zhang, “Deep plug-and-play super-resolution for arbitrary blur kernels,” in *Proc. IEEE Conf. Computer Vision and Pattern Recognition (CVPR)*, Long Beach, CA, USA, June 16-20, 2019, pp. 1671–1681.
- [56] Y. Sun, S. Xu, Y. Li, L. Tian, B. Wohlberg, and U. S. Kamilov, “Regularized Fourier ptychography using an online plug-and-play algorithm,” in *Proc. IEEE Int. Conf. Acoustics, Speech and Signal Process. (ICASSP)*, Brighton, UK, May 12-17, 2019, pp. 7665–7669.
- [57] R. Ahmad, C. A. Bouman, G. T. Buzzard, S. Chan, S. Liu, E. T. Reehorst, and P. Schniter, “Plug-and-play methods for magnetic resonance imaging: Using denoisers for image recovery,” *IEEE Signal Processing Magazine*, vol. 37, no. 1, pp. 105–116, 2020.

- [58] K. Wei, A. Aviles-Rivero, J. Liang, Y. Fu, C.-B. Schönlieb, and H. Huang, “Tuning-free plug-and-play proximal algorithm for inverse imaging problems,” in *Proc. 37th Int. Conf. Machine Learning (ICML)*, 2020.
- [59] M. Xie, J. Liu, Y. Sun, W. Gan, B. Wohlberg, and U. S. Kamilov, “Joint reconstruction and calibration using regularization by denoising with application to computed tomography,” in *Proc. IEEE Int. Conf. Comp. Vis. Workshops (ICCVW)*, October 2021, pp. 4028–4037.
- [60] T. Meinhardt, M. Moeller, C. Hazirbas, and D. Cremers, “Learning proximal operators: Using denoising networks for regularizing inverse imaging problems,” in *Proc. IEEE Int. Conf. Comp. Vis. (ICCV)*, Venice, Italy, Oct. 22-29, 2017, pp. 1799–1808.
- [61] Y. Sun, B. Wohlberg, and U. S. Kamilov, “An online plug-and-play algorithm for regularized image reconstruction,” *IEEE Trans. Comput. Imag.*, vol. 5, no. 3, pp. 395–408, Sept. 2019.
- [62] T. Tirer and R. Giryes, “Image restoration by iterative denoising and backward projections,” *IEEE Trans. Image Process.*, vol. 28, no. 3, pp. 1220–1234, Mar. 2019.
- [63] A. M. Teodoro, J. M. Bioucas-Dias, and M. A. T. Figueiredo, “A convergent image fusion algorithm using scene-adapted Gaussian-mixture-based denoising,” *IEEE Trans. Image Process.*, vol. 28, no. 1, pp. 451–463, Jan. 2019.
- [64] X. Xu, Y. Sun, J. Liu, B. Wohlberg, and U. S. Kamilov, “Provable convergence of plug-and-play priors with mmse denoisers,” *IEEE Signal Process. Lett.*, vol. 27, pp. 1280–1284, 2020.
- [65] Y. Sun, Z. Wu, B. Wohlberg, and U. S. Kamilov, “Scalable plug-and-play ADMM with convergence guarantees,” *IEEE Trans. Comput. Imag.*, vol. 7, pp. 849–863, July 2021.
- [66] R. Cohen, M. Elad, and P. Milanfar, “Regularization by denoising via fixed-point projection (red-pro),” *SIAM Journal on Imaging Sciences*, vol. 14, no. 3, pp. 1374–1406, 2021.
- [67] J. Tang and M. Davies, “A fast stochastic plug-and-play ADMM for imaging inverse problems,” 2020, arXiv:2006.11630.
- [68] V. Monga, Y. Li, and Y. C. Eldar, “Algorithm unrolling: Interpretable, efficient deep learning for signal and image processing,” *IEEE Signal Process. Mag.*, vol. 38, no. 2, pp. 18–44, Mar. 2021.
- [69] M. Kellman, K. Zhang, E. Markley, J. Tamir, E. Bostan, M. Lustig, and L. Waller, “Memory-efficient learning for large-scale computational imaging,” *IEEE Trans. Comp. Imag.*, vol. 6, pp. 1403–1414, 2020.
- [70] J. Liu, Y. Sun, W. Gan, B. Wohlberg, and U. S. Kamilov, “Sgd-net: Efficient model-based deep learning with theoretical guarantees,” *IEEE Transactions on Computational Imaging*, vol. 7, pp. 598–610, 2021.
- [71] Z. Wu, Y. Sun, J. Liu, and U. S. Kamilov, “Online regularization by denoising with applications to phase retrieval,” in *Proc. IEEE Int. Conf. Comput. Vis. Workshops*, Oct. 2019, pp. 1–9.
- [72] Y. Nesterov, *Introductory Lectures on Convex Optimization: A Basic Course*, Kluwer Academic Publishers, 2004.
- [73] P. Jain and P. Kar, “Non-convex optimization for machine learning,” *Foundations and Trends in Machine Learning*, vol. 10, no. 3-4, pp. 142–363, 2017.
- [74] T. Miyato, T. Kataoka, M. Koyama, and Y. Yoshida, “Spectral normalization for generative adversarial networks,” in *Int. Conf. on Learning Representations (ICLR)*, Vancouver, Canada, Apr. 2018.
- [75] D. G Anderson, “Iterative procedures for nonlinear integral equations,” *Journal of the ACM (JACM)*, vol. 12, no. 4, pp. 547–560, 1965.

- [76] S. Bai, V. Koltun, and J. Z. Kolter, “Neural deep equilibrium solvers,” in *International Conference on Learning Representations*, 2022.
- [77] A. Aksac, D. J. Demetrick, T. Ozyer, and R. Alhaji, “Brecahad: a dataset for breast cancer histopathological annotation and diagnosis,” *BMC research notes*, vol. 12, no. 1, pp. 1–3, 2019.
- [78] C. McCollough, “TU-FG-207A-04: Overview of the low dose CT grand challenge,” *Med. Phys.*, vol. 43, no. 6Part35, pp. 3759–3760, 2016.
- [79] D. Kingma and J. Ba, “Adam: A method for stochastic optimization,” in *Proc. Int. Conf. on Learn. Represent.*, 2015.
- [80] M. Lustig, D. L. Donoho, and J. M. Pauly, “Sparse MRI: The application of compressed sensing for rapid MR imaging,” *Magn. Reson. Med.*, vol. 58, no. 6, pp. 1182–1195, Dec. 2007.
- [81] M. Lustig, D. L. Donoho, J. M. Santos, and J. M. Pauly, “Compressed sensing MRI,” *IEEE Signal Process. Mag.*, vol. 25, no. 2, pp. 72–82, Mar. 2008.
- [82] K. P. Pruessmann, M. Weiger, M. B. Scheidegger, and P. Boesiger, “SENSE: Sensitivity encoding for fast MRI,” *Magn. Reson. Med.*, vol. 42, no. 5, pp. 952–962, Nov. 1999.
- [83] F. Knoll *et al.*, “fastMRI: A publicly available raw k-space and DICOM dataset of knee images for accelerated MR image reconstruction using machine learning,” *Radiology: Artificial Intelligence*, vol. 2, no. 1, pp. e190007, 2020.
- [84] F. Ong and M. Lustig, “Sigpy: a python package for high performance iterative reconstruction,” in *Proceedings of the ISMRM 27th Annual Meeting, Montreal, Quebec, Canada*, 2019, vol. 4819.
- [85] U. S. Kamilov, I. N. Papadopoulos, M. H. Shoreh, A. Goy, C. Vonesch, M. Unser, and D. Psaltis, “Optical tomographic image reconstruction based on beam propagation and sparse regularization,” *IEEE Trans. Comp. Imag.*, vol. 2, no. 1, pp. 59–70, Mar. 2016.
- [86] H. H. Bauschke and P. L. Combettes, *Convex Analysis and Monotone Operator Theory in Hilbert Spaces*, Springer, 2 edition, 2017.
- [87] E. K. Ryu and S. Boyd, “A primer on monotone operator methods,” *Appl. Comput. Math.*, vol. 15, no. 1, pp. 3–43, 2016.
- [88] R. T. Rockafellar, *Convex Analysis*, Princeton Univ. Press, Princeton, NJ, 1970.
- [89] S. Boyd and L. Vandenberghe, *Convex Optimization*, Cambridge Univ. Press, 2004.
- [90] Y. Wu and K. He, “Group normalization,” in *Proc. Euro. Conf. Comp. Vis.*, Sep. 2018, pp. 3–19.
- [91] H. Gupta, K. H. Jin, H. Q. Nguyen, M. T. McCann, and M. Unser, “CNN-based projected gradient descent for consistent ct image reconstruction,” *IEEE Trans. Med. Imag.*, vol. 37, no. 6, pp. 1440–1453, Jun. 2018.
- [92] Z. Wang, A. C. Bovik, H. R. Sheikh, and E. P. Simoncelli, “Image quality assessment: from error visibility to structural similarity,” *IEEE Trans. Image Process.*, vol. 13, no. 4, pp. 600–612, Apr 2004.
- [93] L. N. Smith, “Cyclical learning rates for training neural networks,” in *2017 IEEE Winter Conference on Applications of Computer Vision*, Mar. 2017, pp. 464–472.

Supplementary Material

We adopt the monotone operator theory [86, 87] for a unified analysis of ODER. The contributions of this work are algorithmic, theoretical, and numerical. We propose ODER as a new algorithm. We then develop new theoretical insights into its convergence and ability to approximate the traditional DEQ. In Supplement A, we prove the convergence of forward pass for ODER to $\bar{x} \in \text{Fix}(\mathsf{T})$ up to an error term controlled by γ and w . In Supplement B, we prove that the online backward pass in expectation converges to $\bar{b} \in \text{Fix}(\mathsf{F})$ up to an error term that can be controlled via w . In Supplement C, we prove the ability of ODER to approximate the stationary points of the desired loss $\ell(\theta)$ up to an error term that can be controlled during training. Finally, in Section D, we provide additional technical details on our implementations and simulations omitted from the main paper due to space.

We use the same notations as in the main manuscript. The measurement model corresponds to $\mathbf{y} = \mathbf{A}\mathbf{x}^* + \mathbf{e}$, where \mathbf{x}^* is the true solution and \mathbf{e} is the noise. The function $g(\mathbf{x})$ denotes the data-fidelity term. The operator $\mathsf{D}_\theta(\cdot)$ denotes the learned prior within ODER and RED (DEQ), which is implemented via its residual $\mathsf{R}_\theta := \mathsf{I} - \mathsf{D}_\theta$. The operator $\widehat{\mathsf{T}}_\theta(\cdot)$ and $\widehat{\mathsf{F}}(\cdot)$ denote the ODER stochastic forward and backward passes, respectively. The operator $\mathsf{T}_\theta(\cdot)$ and $\mathsf{F}(\cdot)$ denote the full batch forward and backward passes of RED (DEQ), respectively. Finally, our code, including pre-trained CNN models used in ODER and RED (DEQ), is also included in the supplementary material.

A Proof of Theorem 1

The following theorem shows the convergence (in expectation) of the ODER forward pass for convex g and contractive D_θ . Note that this proof is a variation of existing results in the literature on online PnP/RED [21, 61, 65, 67]. However, this result plays an important role in the analysis of both the backward pass and the ability of ODER to approximate the traditional DEQ learning.

Theorem 1. *Run the forward pass of ODER for $k \geq 1$ iterations under Assumptions 1-4 using the step size $0 < \gamma < 1/(\lambda + \tau)$. Then, the sequence of forward pass iterates satisfies*

$$\mathbb{E} [\|\mathbf{x}^k - \bar{\mathbf{x}}\|_2] \leq \eta^k R + \frac{\gamma\nu}{(1 - \eta)\sqrt{w}}, \quad (16)$$

for some constant $0 < \eta < 1$ where $\bar{\mathbf{x}} \in \text{Fix}(\mathsf{T})$.

Proof. For notation connivance, we abbreviate $\mathsf{T}_\theta(\dots)$ as $\mathsf{T}_\theta(\dots)$ in the following proof. From Lemma 1, T is a contraction, which means that there exists $0 < \eta < 1$ such that

$$\|\mathsf{T}(\mathbf{z}) - \mathsf{T}(\mathbf{y})\|_2 \leq \eta \|\mathbf{z} - \mathbf{y}\|_2,$$

for all $\mathbf{z}, \mathbf{y} \in \mathbb{R}^n$. Then, for $\bar{\mathbf{x}} \in \text{Fix}(\mathsf{T})$, we have that

$$\begin{aligned} \|\mathbf{x}^k - \bar{\mathbf{x}}\|_2 &= \|\widehat{\mathsf{T}}(\mathbf{x}^{k-1}) - \mathsf{T}(\bar{\mathbf{x}})\|_2^2 = \|\mathsf{T}(\mathbf{x}^{k-1}) - \mathsf{T}(\bar{\mathbf{x}}) + \widehat{\mathsf{T}}(\mathbf{x}^{k-1}) - \mathsf{T}(\mathbf{x}^{k-1})\|_2^2 \\ &\leq \|\mathsf{T}(\mathbf{x}^{k-1}) - \mathsf{T}(\bar{\mathbf{x}})\|_2 + \gamma \|\mathsf{T}(\mathbf{x}^{k-1}) - \widehat{\mathsf{T}}(\mathbf{x}^{k-1})\|_2 \\ &\leq \eta \|\mathbf{x}^{k-1} - \bar{\mathbf{x}}\|_2 + \|\nabla g(\mathbf{x}^{k-1}) - \nabla \widehat{g}(\mathbf{x}^{k-1})\|_2, \end{aligned}$$

where we used the triangular inequality and that T is η -Lipschitz continuous. We take the conditional expectation from both sides to obtain

$$\mathbb{E} [\|\mathbf{x}^k - \bar{\mathbf{x}}\|_2 \mid \mathbf{x}^{k-1}] \leq \eta \|\mathbf{x}^{k-1} - \bar{\mathbf{x}}\|_2 + \frac{\gamma\nu}{\sqrt{w}},$$

where we applied the Jensen's inequality to the variance bound in Assumption 4. By taking the total expectation, we thus have

$$\mathbb{E} [\|\mathbf{x}^k - \bar{\mathbf{x}}\|_2] \leq \eta \mathbb{E} [\|\mathbf{x}^{k-1} - \bar{\mathbf{x}}\|_2] + \frac{\gamma\nu}{\sqrt{w}}.$$

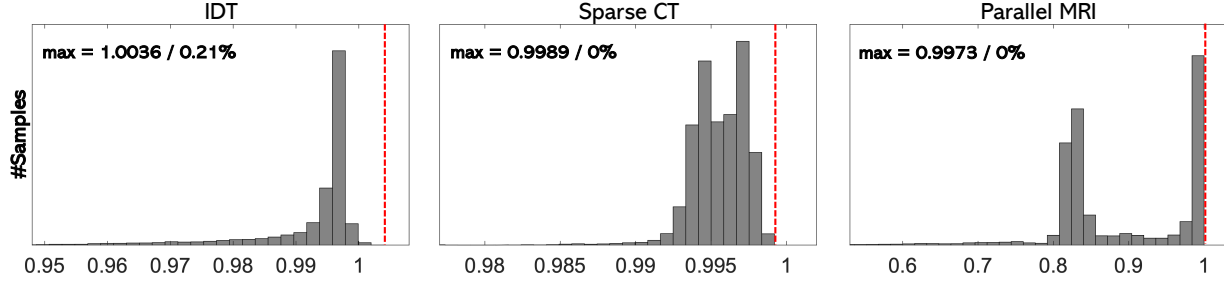


Figure 4: Empirical evaluation of the Lipschitz continuity of T . Each histogram was generated by storing all ODER iterates and $\bar{\mathbf{x}} \in \text{Fix}(\mathsf{T})$ across all the test images used in the tables of the main paper. The x-axis is the value of $\|\mathsf{T}(\mathbf{x}^{k-1}) - \mathsf{T}(\bar{\mathbf{x}})\|_2 / \|\mathbf{x}^{k-1} - \bar{\mathbf{x}}\|_2$. **Left:** The histogram of IDT at $b = 500$ with $\{15, 20, 25\}$ dB of input SNR. **Middle:** The histogram of sparse CT at $b \in \{90, 120, 180\}$ projection views. **Right:** The histogram of the radially sub-sampled parallel MRI at 10% and 20% sampling. Note how T numerically acts as a contraction on all the iterates generated for the CT and MRI experiments, and on 99.79% iterates generated for the IDT experiments. Despite their imperfect numerical precision, current spectral normalization techniques still provide a powerful tool for systematically ensuring stability of PnP/RED fixed-point iterations.

By iterating this inequality and using the bound in Assumption 3, we get the result

$$\mathbb{E} [\|\mathbf{x}^k - \bar{\mathbf{x}}\|_2] \leq \eta^k R + \frac{\gamma\nu}{(1-\eta)\sqrt{w}}.$$

□

A.1 Useful Results for the Proof of Theorem 1

The following lemma establishes that T is a contraction. The proof is a minor modification of the Theorem 1 from [35], which we provide for completeness. It is worth noting that this result does not assume that the functions $\{g_i\}$ are strongly convex.

Lemma 1. *Suppose that Assumptions 1-2 in the main paper are true. Then, for any $0 < \gamma < 1/(\lambda + \tau)$, the operator T in eq. (2) of the main paper is a contraction, which means that for all $\mathbf{x} \in \mathbb{R}^n$*

$$\|\nabla_{\mathbf{x}}\mathsf{T}(\mathbf{x})\|_2 < 1,$$

where $\|\cdot\|_2$ denotes the spectral norm.

Proof. The Jacobian of the operator T with respect to \mathbf{x} is given by

$$\nabla_{\mathbf{x}}\mathsf{T}(\mathbf{x}) = (1 - \gamma\tau)\mathbf{I} - \gamma\mathsf{H}g(\mathbf{x}) - \gamma\tau\nabla_{\mathbf{x}}\mathsf{D}(\mathbf{x}).$$

Let $\lambda_1 \geq \dots \geq \lambda_n$ denote sorted eigenvalues of the Hessian matrix $\mathsf{H}g(\mathbf{x})$. Since g is convex, we have that $\lambda_n \geq 0$. Then, for any $\mathbf{x} \in \mathbb{R}^n$, we have

$$\begin{aligned} \|\nabla_{\mathbf{x}}\mathsf{T}(\mathbf{x})\|_2 &= \|(1 - \gamma\tau)\mathbf{I} - \gamma\mathsf{H}g(\mathbf{x}) - \gamma\tau\nabla_{\mathbf{x}}\mathsf{D}(\mathbf{x})\|_2 \\ &\leq \|(1 - \gamma\tau)\mathbf{I} - \gamma\mathsf{H}g(\mathbf{x})\|_2 + \gamma\tau\|\nabla_{\mathbf{x}}\mathsf{D}(\mathbf{x})\|_2 \\ &\leq \max_{1 \leq i \leq n} \{1 - \gamma\tau - \gamma\lambda_i\} + \gamma\tau\kappa \\ &\leq 1 - \gamma\tau(1 - \kappa) < 1, \end{aligned}$$

where in the first inequality we used the triangular inequality, in the second the fact that D is a contraction, and in the third the convexity of g . □

B Proof of Theorem 2

The following result is a novel analysis of the ODER backward pass. The result implies that the backward pass converges (in expectation) up to an error term that can be controlled by the minibatch parameter w . Our numerical results provide additional corroboration to our theory by showing that ODER nearly matches the performance of the traditional DEQ learning.

Theorem 2. *Run the backward pass of ODER for $k \geq 1$ iterations under Assumptions 1-4 from $\mathbf{b}^0 = \mathbf{0}$ using the step-size $0 < \gamma < 1/(\lambda + \tau)$. Then, the sequence of backward pass iterates satisfies*

$$\mathbb{E} [\|\mathbf{b}^k - \bar{\mathbf{b}}\|_2] \leq B_1 \eta^k + \frac{B_2}{\sqrt{w}}, \quad (17)$$

where $0 < \eta < 1$, $B_1 > 0$ and $B_2 > 0$ are constants independent of k and w , and $\bar{\mathbf{b}} \in \text{Fix}(\mathbf{F})$.

Proof. Let \mathbf{x}^K denote the output of the forward pass of ODER after $K \geq 1$ iterations, \mathbf{x}^* denote the training label, and $\bar{\mathbf{x}} \in \text{Fix}(\mathbf{T})$. Consider the following two operators

$$\mathbf{F}(\mathbf{b}) = [\nabla_{\mathbf{x}} \mathbf{T}(\bar{\mathbf{x}})]^T \mathbf{b} + (\bar{\mathbf{x}} - \mathbf{x}^*) \quad \text{and} \quad \hat{\mathbf{F}}(\mathbf{b}) = [\nabla_{\mathbf{x}} \hat{\mathbf{T}}(\mathbf{x}^K)]^T \mathbf{b} + (\mathbf{x}^K - \mathbf{x}^*),$$

where the first operator is used in the backward pass of RED (DEQ), while the second is its online approximation. Note also the following two Jacobians

$$\nabla_{\mathbf{x}} \mathbf{T}(\bar{\mathbf{x}}) = \mathbf{I} - \gamma(\mathbf{H}g(\bar{\mathbf{x}}) + \tau \nabla_{\mathbf{x}} \mathbf{R}(\bar{\mathbf{x}})) \quad \text{and} \quad \nabla_{\mathbf{x}} \hat{\mathbf{T}}(\mathbf{x}^K) = \mathbf{I} - \gamma(\mathbf{H}\hat{g}(\mathbf{x}^K) + \tau \nabla_{\mathbf{x}} \mathbf{R}(\mathbf{x}^K)).$$

Lemma 1 implies that \mathbf{T} is a contraction. Let $0 < \eta < 1$ denote the Lipschitz constant of \mathbf{T} . Since $\nabla_{\mathbf{b}} \mathbf{F}(\mathbf{b}) = \nabla_{\mathbf{x}} \mathbf{T}(\bar{\mathbf{x}})$, we have $\|\nabla_{\mathbf{b}} \mathbf{F}(\mathbf{b})\|_2 = \|\nabla_{\mathbf{x}} \mathbf{T}(\bar{\mathbf{x}})\|_2 \leq \eta$, which means that \mathbf{F} is a contraction

$$\|\mathbf{F}(\mathbf{z}) - \mathbf{F}(\mathbf{y})\|_2 \leq \eta \|\mathbf{z} - \mathbf{y}\|_2, \quad \mathbf{z}, \mathbf{y} \in \mathbb{R}^n.$$

We can thus show the following bound

$$\begin{aligned} \|\mathbf{b}^k - \bar{\mathbf{b}}\|_2 &= \|\hat{\mathbf{F}}(\mathbf{b}^{k-1}) - \mathbf{F}(\bar{\mathbf{b}})\|_2 = \|\mathbf{F}(\mathbf{b}^{k-1}) - \mathbf{F}(\bar{\mathbf{b}}) + \hat{\mathbf{F}}(\mathbf{b}^{k-1}) - \mathbf{F}(\mathbf{b}^{k-1})\|_2 \\ &\leq \|\mathbf{F}(\mathbf{b}^{k-1}) - \mathbf{F}(\bar{\mathbf{b}})\|_2 + \|\hat{\mathbf{F}}(\mathbf{b}^{k-1}) - \mathbf{F}(\mathbf{b}^{k-1})\|_2 \\ &\leq \eta \|\mathbf{b}^{k-1} - \bar{\mathbf{b}}\|_2 + \|\hat{\mathbf{F}}(\mathbf{b}^{k-1}) - \mathbf{F}(\mathbf{b}^{k-1})\|_2, \end{aligned}$$

where we first used the triangular inequality and then the fact that \mathbf{F} is a contraction. By taking the conditional expectation on both sides, we obtain

$$\mathbb{E} [\|\mathbf{b}^k - \bar{\mathbf{b}}\|_2 \mid \mathbf{x}^K, \mathbf{b}^{k-1}] \leq \eta \|\mathbf{b}^{k-1} - \bar{\mathbf{b}}\|_2 + \mathbb{E} [\|\hat{\mathbf{F}}(\mathbf{b}^{k-1}) - \mathbf{F}(\mathbf{b}^{k-1})\|_2 \mid \mathbf{x}^K, \mathbf{b}^{k-1}]. \quad (18)$$

We can bound the second term in (18) as follows

$$\begin{aligned} \mathbb{E} [\|\hat{\mathbf{F}}(\mathbf{b}^{k-1}) - \mathbf{F}(\mathbf{b}^{k-1})\|_2 \mid \mathbf{x}^K, \mathbf{b}^{k-1}] &\leq \gamma \mathbb{E} [\|\mathbf{H}g(\bar{\mathbf{x}}) - \mathbf{H}\hat{g}(\mathbf{x}^K)\|_2 \mid \mathbf{x}^K, \mathbf{b}^{k-1}] \|\mathbf{b}^{k-1}\|_2 \\ &\quad + \gamma \tau \|\nabla_{\mathbf{x}} \mathbf{R}(\bar{\mathbf{x}}) - \nabla_{\mathbf{x}} \mathbf{R}(\mathbf{x}^K)\|_2 \|\mathbf{b}^{k-1}\|_2 + \|\mathbf{x}^K - \bar{\mathbf{x}}\|_2 \\ &\leq \gamma \lambda \|\mathbf{x}^K - \bar{\mathbf{x}}\|_2 \|\mathbf{b}^{k-1}\|_2 + \frac{\gamma \nu}{\sqrt{w}} \|\mathbf{b}^{k-1}\|_2 + \gamma \tau \alpha \|\mathbf{x}^K - \bar{\mathbf{x}}\|_2 \|\mathbf{b}^{k-1}\|_2 + \|\mathbf{x}^K - \bar{\mathbf{x}}\|_2 \\ &\leq A_1 \|\mathbf{x}^K - \bar{\mathbf{x}}\|_2 + \frac{A_2}{\sqrt{w}}, \end{aligned}$$

with $A_1 := (2\gamma\lambda + 2\gamma\tau\alpha R + 1)$ and $A_2 = 2\nu R$, where in the second inequality we used Lemma 2 and the α -Lipschitz continuity of $\nabla_{\mathbf{x}} \mathbf{R}$ and in the third $\|\mathbf{b}^{k-1}\|_2 \leq 2R$. Since $\mathbf{b}^0 = \mathbf{0}$, Assumption 3 implies that $\|\bar{\mathbf{b}}\|_2 \leq R$, which leads to $\|\mathbf{b}^{k-1}\|_2 \leq 2R$ for all $k \geq 1$.

By including the last bound into (18), we obtain

$$\mathbb{E} [\|\mathbf{b}^k - \bar{\mathbf{b}}\|_2 \mid \mathbf{x}^K, \mathbf{b}^{k-1}] \leq \eta \|\mathbf{b}^{k-1} - \bar{\mathbf{b}}\|_2 + A_1 \|\mathbf{x}^K - \bar{\mathbf{x}}\|_2 + A_2 / \sqrt{w}.$$

By taking the total expectation and using Theorem 1, we get

$$\mathbb{E} [\|\mathbf{b}^k - \bar{\mathbf{b}}\|_2] \leq \eta \mathbb{E} [\|\mathbf{b}^{k-1} - \bar{\mathbf{b}}\|_2] + A_1 R \eta^K + \frac{A_1 \gamma \nu}{(1 - \nu) \sqrt{w}} + \frac{A_2}{\sqrt{w}}.$$

By iterating this bound and noting that $k \leq K$, we get the final result

$$\mathbb{E} [\|\mathbf{b}^k - \bar{\mathbf{b}}\|_2] \leq \eta^k B_1 + \frac{B_2}{\sqrt{w}},$$

where $B_1 := R + A_1 R / (1 - \eta)$ and $B_2 := (((A_1 \gamma \nu) / (1 - \eta)) + A_2) / (1 - \nu)$. □

B.1 Technical Lemma for the Proof of Theorem 2

The following technical result is used in the proof of Theorem 2. It bounds the variance of the Hessian of the data-fidelity term g .

Lemma 2. *Suppose that Assumptions 1 and 4 in the main paper are true. Then, for any $\mathbf{z}, \mathbf{y} \in \mathbb{R}^n$*

$$\mathbb{E} [\|\mathbb{H}g(\mathbf{z}) - \mathbb{H}\hat{g}(\mathbf{y})\|_2] \leq \lambda \|\mathbf{z} - \mathbf{y}\|_2 + \frac{\nu}{\sqrt{w}},$$

where the expectation is taken over the indices $\{i_1, \dots, i_w\}$ used for \hat{g} .

Proof. The proof directly follows the λ -Lipschitz continuity assumption of $\mathbb{H}g$ is Assumption 1 and boundedness of the variance in Assumption 4

$$\begin{aligned} \mathbb{E} [\|\mathbb{H}g(\mathbf{z}) - \mathbb{H}\hat{g}(\mathbf{y})\|_2] &\leq \mathbb{E} [\|\mathbb{H}g(\mathbf{z}) - \mathbb{H}g(\mathbf{y})\|_2] + \mathbb{E} [\|\mathbb{H}g(\mathbf{y}) - \mathbb{H}\hat{g}(\mathbf{y})\|_2] \\ &\leq \lambda \|\mathbf{z} - \mathbf{y}\|_2 + \frac{\nu}{\sqrt{w}}, \end{aligned}$$

where we used the Jensen's inequality to get the second term. □

C Proof of Theorem 3

Our final theoretical result is a novel analysis on the ability of ODER to approximate the stationary points of the loss $\ell(\boldsymbol{\theta})$. We show that ODER can approximate (in expectation) the stationary points up to an error term that can be controlled by the minibatch size w and the learning rate β .

Theorem 3. *Train ODER using SGD for $T \geq 1$ iterations under Assumptions 1-6 using the step-size parameters $0 < \beta \leq 1/L$ and the minibatch size $w \geq 1$. Select a large enough number of forward and backward pass iterations $K \geq 1$ to satisfy $0 < \eta^K \leq 1/\sqrt{w}$. Then, we have that*

$$\frac{1}{T} \sum_{t=0}^{T-1} \mathbb{E} [\|\nabla \ell(\boldsymbol{\theta}^t)\|_2^2] \leq \frac{2(\ell(\boldsymbol{\theta}^0) - \ell(\boldsymbol{\theta}^*))}{\beta T} + \frac{C_1}{\sqrt{w}} + \beta C_2.$$

where $C_1 > 0$ and $C_2 > 0$ are constants independent of T and w .

Proof. Consider the RED (DEQ) loss ℓ and its ODER approximation $\hat{\ell}$

$$\ell(\boldsymbol{\theta}) = \frac{1}{p} \sum_{j=1}^p \ell_j(\boldsymbol{\theta}) \quad \text{and} \quad \hat{\ell}(\boldsymbol{\theta}) = \frac{1}{p} \sum_{j=1}^p \hat{\ell}_j(\boldsymbol{\theta}), \quad (19)$$

where each ℓ_j and $\hat{\ell}_j$ have the forms

$$\ell_j(\boldsymbol{\theta}) = \frac{1}{2} \|\bar{\mathbf{x}}_j(\boldsymbol{\theta}) - \mathbf{x}_j^*\|_2^2 \quad \text{and} \quad \hat{\ell}_j(\boldsymbol{\theta}) = \frac{1}{2} \|\mathbf{x}_j^K(\boldsymbol{\theta}) - \mathbf{x}_j^*\|_2^2.$$

Vector \mathbf{x}_j^K denotes the final iterate of the online forward pass obtained after $K \geq 1$ iterations for the training sample $j \in \{1, \dots, p\}$.

From Assumption 5, we obtain the traditional Lipschitz continuity bound on the gradient

$$\|\nabla \ell(\boldsymbol{\theta}_1) - \nabla \ell(\boldsymbol{\theta}_2)\|_2 \leq L \|\boldsymbol{\theta}_1 - \boldsymbol{\theta}_2\|_2,$$

which directly leads to traditional quadratic upper bound (see Lemma 1.2.3 in [72]).

$$\ell(\boldsymbol{\theta}_1) \leq \ell(\boldsymbol{\theta}_2) + \nabla \ell(\boldsymbol{\theta}_2)^\top (\boldsymbol{\theta}_1 - \boldsymbol{\theta}_2) + \frac{L}{2} \|\boldsymbol{\theta}_1 - \boldsymbol{\theta}_2\|_2^2. \quad (20)$$

Lemma 3 in this supplement establishes the following useful bound for our analysis

$$\mathbb{E} \left[\|\nabla \hat{\ell}(\boldsymbol{\theta}^t) - \nabla \ell(\boldsymbol{\theta}^t)\|_2^2 \right] \leq \frac{C}{\sqrt{w}},$$

for some constant $C > 0$ (see its full expression in Lemma 3). This directly implies that

$$\mathbb{E} \left[-\nabla \ell(\boldsymbol{\theta}^t)^\top \nabla \hat{\ell}(\boldsymbol{\theta}^t) + \frac{1}{2} \|\nabla \hat{\ell}(\boldsymbol{\theta}^t)\|_2^2 \right] \leq -\frac{1}{2} \mathbb{E} [\|\nabla \ell(\boldsymbol{\theta}^t)\|_2^2] + \frac{C}{2\sqrt{w}}. \quad (21)$$

Consider a single iteration of SGD for optimizing ODER

$$\boldsymbol{\theta}^{t+1} = \boldsymbol{\theta}^t - \beta \nabla \hat{\ell}_{j_t}(\boldsymbol{\theta}^t). \quad (22)$$

From the quadratic upper bound (20), we get

$$\begin{aligned} \ell(\boldsymbol{\theta}^{t+1}) - \ell(\boldsymbol{\theta}^t) &\leq \nabla \ell(\boldsymbol{\theta}^t)^\top (\boldsymbol{\theta}^{t+1} - \boldsymbol{\theta}^t) + \frac{L}{2} \|\boldsymbol{\theta}^{t+1} - \boldsymbol{\theta}^t\|_2^2 \\ &= -\beta \nabla \ell(\boldsymbol{\theta}^t)^\top \nabla \hat{\ell}_{j_t}(\boldsymbol{\theta}^t) + \frac{\beta^2 L}{2} \|\nabla \hat{\ell}_{j_t}(\boldsymbol{\theta}^t)\|_2^2. \end{aligned}$$

For notation convenience, we use $\mathbb{E}[\cdot | j_t]$ to denote the expectation only with respect to the training index $j_t \in \{1, \dots, p\}$, where we condition on $\boldsymbol{\theta}^t$ and the random indices within forward and backward passes at this iteration. By taking $\mathbb{E}[\cdot | j_t]$ on both sides of the quadratic upper bound (20)

$$\begin{aligned} \mathbb{E} [\ell(\boldsymbol{\theta}^{t+1}) | j_t] - \ell(\boldsymbol{\theta}^t) &\leq -\beta \nabla \ell(\boldsymbol{\theta}^t)^\top \mathbb{E} [\nabla \hat{\ell}_{j_t}(\boldsymbol{\theta}^t) | j_t] + \frac{\beta^2 L}{2} \mathbb{E} [\|\nabla \hat{\ell}_{j_t}(\boldsymbol{\theta}^t)\|_2^2 | j_t] \\ &= -\beta \nabla \ell(\boldsymbol{\theta}^t)^\top \nabla \hat{\ell}(\boldsymbol{\theta}^t) + \frac{\beta^2 L}{2} \mathbb{E} [\|\nabla \hat{\ell}_{j_t}(\boldsymbol{\theta}^t)\|_2^2 | j_t], \end{aligned} \quad (23)$$

where we use (19) and the fact that j_t is distributed uniformly at random in $\{1, \dots, p\}$.

We now estimate the last term in (23)

$$\begin{aligned} &\mathbb{E} \left[\|\nabla \hat{\ell}_{j_t}(\boldsymbol{\theta}^t)\|_2^2 | j_t \right] \\ &= \mathbb{E} \left[\|\nabla \hat{\ell}_{j_t}(\boldsymbol{\theta}^t) - \nabla \hat{\ell}(\boldsymbol{\theta}^t) + \nabla \hat{\ell}(\boldsymbol{\theta}^t)\|_2^2 | j_t \right] \\ &= \mathbb{E} \left[\|\nabla \hat{\ell}_{j_t}(\boldsymbol{\theta}^t) - \nabla \hat{\ell}(\boldsymbol{\theta}^t)\|_2^2 + 2(\nabla \hat{\ell}_{j_t}(\boldsymbol{\theta}^t) - \nabla \hat{\ell}(\boldsymbol{\theta}^t))^\top \nabla \hat{\ell}(\boldsymbol{\theta}^t) + \|\nabla \hat{\ell}(\boldsymbol{\theta}^t)\|_2^2 | j_t \right] \\ &= \mathbb{E} \left[\|\nabla \hat{\ell}_{j_t}(\boldsymbol{\theta}^t) - \nabla \hat{\ell}(\boldsymbol{\theta}^t)\|_2^2 | j_t \right] + \mathbb{E} \left[\|\nabla \hat{\ell}(\boldsymbol{\theta}^t)\|_2^2 | j_t \right], \end{aligned} \quad (24)$$

where in the third equality we use the fact that $\mathbb{E} \left[(\nabla \hat{\ell}_{j_t}(\boldsymbol{\theta}^t) - \nabla \hat{\ell}(\boldsymbol{\theta}^t))^\top \nabla \hat{\ell}(\boldsymbol{\theta}^t) \mid \setminus j_t \right] = 0$.

By replacing the last term in (23) with (24) and taking the full expectation on both sides of (23) in terms of all random variables and invoking the bound (21), we obtain

$$\begin{aligned} & \mathbb{E}[\ell(\boldsymbol{\theta}^{t+1})] - \mathbb{E}[\ell(\boldsymbol{\theta}^t)] \\ & \leq \mathbb{E} \left[-\beta \nabla \ell(\boldsymbol{\theta}^t)^\top \nabla \hat{\ell}(\boldsymbol{\theta}^t) + \frac{\beta^2 L}{2} \|\nabla \hat{\ell}(\boldsymbol{\theta}^t)\|^2 \right] + \frac{\beta^2 L}{2} \mathbb{E} \left[\|\nabla \hat{\ell}_{j_t}(\boldsymbol{\theta}^t) - \nabla \hat{\ell}(\boldsymbol{\theta}^t)\|_2^2 \right] \\ & \leq -\frac{\beta}{2} \mathbb{E}[\|\nabla \ell(\boldsymbol{\theta}^t)\|_2^2] + \frac{\beta C}{2\sqrt{w}} + \frac{\beta^2 L}{2} (4\sigma^2 + \frac{6C}{\sqrt{w}}), \end{aligned}$$

where we used the fact that $0 < \beta \leq 1/L$, and in the last inequality we used the bound from Lemma 4 in this document. By rearranging the terms, and summing this bound over $0 \leq t \leq T-1$, we obtain

$$\begin{aligned} \frac{1}{T} \sum_{t=0}^{T-1} \mathbb{E}[\|\nabla \ell(\boldsymbol{\theta}^t)\|_2^2] & \leq \frac{2(\ell(\boldsymbol{\theta}^0) - \mathbb{E}[\ell(\boldsymbol{\theta}^T)])}{\beta T} + \frac{C_1}{\sqrt{w}} + \beta C_2 \\ & \leq \frac{2(\ell(\boldsymbol{\theta}^0) - \ell(\boldsymbol{\theta}^*))}{\beta T} + \frac{C_1}{\sqrt{w}} + \beta C_2, \end{aligned}$$

where $C_1 := 7\gamma^2\tau^2\alpha^2(R+R^2)(B_1+B_2+R^2+\gamma\nu R/(1-\eta))$ and $C_2 := 4L\sigma^2$ are constants independent of t and w . In the last inequality we used the fact that $\ell(\boldsymbol{\theta}^*) \leq \ell(\boldsymbol{\theta})$ for all $\boldsymbol{\theta}$, where $\boldsymbol{\theta}^*$ denotes a global minimizer of ℓ . \square

C.1 Technical Lemmas for the Proof of Theorem 3

The following lemma are useful for relating $\nabla \hat{\ell}$ and $\nabla \ell$ in expectation up to an error term. Both are used in the proof of Theorem 3.

Lemma 3. *Given the loss function ℓ of RED (DEQ) and $\hat{\ell}$ of ODER, by selecting a large enough number of forward and backward iterations $K \geq 1$ to satisfy $0 < \eta^K \leq 1/\sqrt{w}$, we have*

$$\mathbb{E} \left[\|\nabla \hat{\ell}(\boldsymbol{\theta}) - \nabla \ell(\boldsymbol{\theta})\|_2^2 \right] \leq \frac{C}{\sqrt{w}},$$

where $C := \gamma^2\tau^2\alpha^2(R+R^2)(B_1+B_2+R^2+\gamma\nu R/(1-\eta))$ is a constant.

Proof. By using the DEQ training, we have the following bound

$$\begin{aligned} \|\nabla \hat{\ell}_j(\boldsymbol{\theta}) - \nabla \ell_j(\boldsymbol{\theta})\|_2 & = \left\| \left[\nabla_{\boldsymbol{\theta}} \hat{\mathbf{T}}_{\boldsymbol{\theta}}(\mathbf{x}_j^K) \right]^\top \mathbf{b}_j^K - \left[\nabla_{\boldsymbol{\theta}} \mathbf{T}_{\boldsymbol{\theta}}(\bar{\mathbf{x}}_j) \right]^\top \bar{\mathbf{b}}_j \right\|_2 \\ & = \left\| \left[\nabla_{\boldsymbol{\theta}} \hat{\mathbf{T}}_{\boldsymbol{\theta}}(\mathbf{x}_j^K) \right]^\top (\mathbf{b}_j^K - \bar{\mathbf{b}}_j) + \left[\nabla_{\boldsymbol{\theta}} \hat{\mathbf{T}}_{\boldsymbol{\theta}}(\mathbf{x}_j^K) - \nabla_{\boldsymbol{\theta}} \mathbf{T}_{\boldsymbol{\theta}}(\bar{\mathbf{x}}_j) \right]^\top \bar{\mathbf{b}}_j \right\|_2 \\ & \leq \left\| \nabla_{\boldsymbol{\theta}} \hat{\mathbf{T}}_{\boldsymbol{\theta}}(\mathbf{x}_j^K) \right\|_2 \|\mathbf{b}_j^K - \bar{\mathbf{b}}_j\|_2 + \left\| \nabla_{\boldsymbol{\theta}} \hat{\mathbf{T}}_{\boldsymbol{\theta}}(\mathbf{x}_j^K) - \nabla_{\boldsymbol{\theta}} \mathbf{T}_{\boldsymbol{\theta}}(\bar{\mathbf{x}}_j) \right\|_2 \|\bar{\mathbf{b}}_j\|_2 \\ & \leq \gamma\tau\alpha(\|\mathbf{b}_j^K - \bar{\mathbf{b}}_j\|_2 + \|\mathbf{x}_j^K - \bar{\mathbf{x}}_j\|_2 \|\bar{\mathbf{b}}_j\|_2), \quad \forall j \in \{1, \dots, p\}, \end{aligned} \tag{25}$$

where in the first inequality, we used Cauchy-Schwarz inequality and the fact that $D_{\boldsymbol{\theta}}$ and $\nabla_{\boldsymbol{\theta}} D_{\boldsymbol{\theta}}(\mathbf{x})$ are α -Lipschitz continuous with respect to \mathbf{x} and $\boldsymbol{\theta}$ based on Assumption 2. By applying Assumption 3 which states that $\|\mathbf{b}^k - \bar{\mathbf{b}}\|_2 < R$ and $\|\mathbf{x}^k - \bar{\mathbf{x}}\|_2 < R$ for every $\mathbf{x}, \mathbf{b} \in \mathbb{R}^n$, we have

$$\|\nabla \hat{\ell}_j(\boldsymbol{\theta}) - \nabla \ell_j(\boldsymbol{\theta})\|_2 \leq \gamma\tau\alpha(R+R^2), \quad \forall j \in \{1, \dots, p\} \tag{26}$$

On the other hand, by taking the expectation with respect to the stochastic approximation variables in forward and backward propagation in (25), invoking the bounds obtained from Theorem 1 and Theorem 2 and using the fact that $0 < \eta^K \leq 1/\sqrt{w}$, we have

$$\mathbb{E} \left[\|\nabla \hat{\ell}_j(\boldsymbol{\theta}) - \nabla \ell_j(\boldsymbol{\theta})\|_2 \right] \leq \gamma\tau\alpha \left(\frac{B_1 + B_2 + R^2}{\sqrt{w}} + \frac{\gamma\nu R}{(1-\eta)\sqrt{w}} \right)$$

where $B_1 > 0$ and $B_2 > 0$ are constants obtained in Theorem 2. Now consider a random variable X which has a probability density function given by $f(x)$ on the real number line such that $P(0 \leq X \leq c) = 1$, then we have

$$\mathbb{E}[X] = \int_0^c x^2 f(x) dx \leq \int_0^c cx f(x) dx = c\mathbb{E}[X].$$

As a consequence, given the bound (26) for the random variables $\|\nabla \hat{\ell}_j(\boldsymbol{\theta}) - \nabla \ell_j(\boldsymbol{\theta})\|_2$ and using the above fact, we have the following useful bound for our proof

$$\mathbb{E} \left[\|\nabla \hat{\ell}_j(\boldsymbol{\theta}) - \nabla \ell_j(\boldsymbol{\theta})\|_2^2 \right] \leq \frac{C}{\sqrt{w}}, \quad (27)$$

where $C := \gamma^2\tau^2\alpha^2(R + R^2)(B_1 + B_2 + R^2 + \gamma\nu R/(1-\eta))$ is a constant.

Note also the fact that for $\mathbf{a}_1, \dots, \mathbf{a}_p \in \mathbb{R}^n$, we have

$$\left\| \sum_{j=1}^p \mathbf{a}_j \right\|_2^2 \leq p \sum_{j=1}^p \|\mathbf{a}_j\|_2^2.$$

As a result, applying the bound (27), we have

$$\begin{aligned} \mathbb{E} \left[\|\nabla \hat{\ell}(\boldsymbol{\theta}) - \nabla \ell(\boldsymbol{\theta})\|_2^2 \right] &= \frac{1}{p^2} \mathbb{E} \left[\left\| \sum_{j=1}^p (\nabla \hat{\ell}_j(\boldsymbol{\theta}) - \nabla \ell_j(\boldsymbol{\theta})) \right\|_2^2 \right] \\ &\leq \frac{1}{p} \sum_{j=1}^p \mathbb{E} \left[\|\nabla \hat{\ell}_j(\boldsymbol{\theta}) - \nabla \ell_j(\boldsymbol{\theta})\|_2^2 \right] \\ &\leq \frac{C}{\sqrt{w}}. \end{aligned}$$

This finishes the proof. □

Lemma 4. Given the loss function ℓ and $\hat{\ell}$, by taking the conditional expectation with respect to the training index j_t (via conditioning on all other variables), we have

$$\mathbb{E} \left[\|\nabla \hat{\ell}_{j_t}(\boldsymbol{\theta}^t) - \nabla \hat{\ell}(\boldsymbol{\theta}^t)\|_2^2 \right] \leq 4\sigma^2 + \frac{6C}{\sqrt{w}},$$

where $C > 0$ obtained in Lemma 3 is a constant.

Proof. By taking expectation with respect to training index $j_t \in \{1, \dots, N\}$, we obtain the following useful

bound for our proof

$$\begin{aligned}
& \mathbb{E} \left[\|\nabla \ell_{j_t}(\boldsymbol{\theta}^t) - \nabla \hat{\ell}(\boldsymbol{\theta}^t)\|_2^2 \mid j_t \right] \\
&= \mathbb{E} \left[\|\nabla \ell_{j_t}(\boldsymbol{\theta}^t) - \nabla \ell(\boldsymbol{\theta}^t) + \nabla \ell(\boldsymbol{\theta}^t) - \nabla \hat{\ell}(\boldsymbol{\theta}^t)\|_2^2 \mid j_t \right] \\
&= \mathbb{E} \left[\|\nabla \ell_{j_t}(\boldsymbol{\theta}^t) - \nabla \ell(\boldsymbol{\theta}^t)\|_2^2 + \|\nabla \ell(\boldsymbol{\theta}^t) - \nabla \hat{\ell}(\boldsymbol{\theta}^t)\|_2^2 \right. \\
&\quad \left. + 2(\nabla \ell_{j_t}(\boldsymbol{\theta}^t) - \nabla \ell(\boldsymbol{\theta}^t))^\top (\nabla \ell(\boldsymbol{\theta}^t) - \nabla \hat{\ell}(\boldsymbol{\theta}^t)) \mid j_t \right] \\
&\leq 2 \left(\mathbb{E} \left[\|\nabla \ell_{j_t}(\boldsymbol{\theta}^t) - \nabla \ell(\boldsymbol{\theta}^t)\|_2^2 + \|\nabla \ell(\boldsymbol{\theta}^t) - \nabla \hat{\ell}(\boldsymbol{\theta}^t)\|_2^2 \mid j_t \right] \right) \\
&= 2\mathbb{E} \left[\|\nabla \ell_{j_t}(\boldsymbol{\theta}^t) - \nabla \ell(\boldsymbol{\theta}^t)\|_2^2 \mid j_t \right] + 2\|\nabla \ell(\boldsymbol{\theta}^t) - \nabla \hat{\ell}(\boldsymbol{\theta}^t)\|_2^2,
\end{aligned} \tag{28}$$

where we used Young's inequality that states for any $\mathbf{a}_1, \mathbf{a}_2 \in \mathbb{R}^n$, we have

$$2\mathbf{a}_1^\top \mathbf{a}_2 \leq \|\mathbf{a}_1\|_2^2 + \|\mathbf{a}_2\|_2^2 \quad \Rightarrow \quad \|\mathbf{a}_1 + \mathbf{a}_2\|_2^2 \leq 2(\|\mathbf{a}_1\|_2^2 + \|\mathbf{a}_2\|_2^2).$$

By taking the full expectation of the inequality (13) above and applying Lemma 3 and the bounded variance in Assumption 6, we have

$$\begin{aligned}
& \mathbb{E} \left[\|\nabla \ell_{j_t}(\boldsymbol{\theta}^t) - \nabla \hat{\ell}(\boldsymbol{\theta}^t)\|_2^2 \right] \\
&\leq 2\mathbb{E} \left[\mathbb{E} \left[\|\nabla \ell_{j_t}(\boldsymbol{\theta}^t) - \nabla \ell(\boldsymbol{\theta}^t)\|_2^2 \mid j_t \right] \right] + 2\mathbb{E} \left[\|\nabla \hat{\ell}(\boldsymbol{\theta}^t) - \nabla \ell(\boldsymbol{\theta}^t)\|_2^2 \right] \\
&\leq 2\sigma^2 + \frac{2C}{\sqrt{w}}
\end{aligned} \tag{29}$$

Similarly, by taking full expectation and using Lemma 3 and the bound (29), we write that

$$\begin{aligned}
& \mathbb{E} \left[\|\nabla \hat{\ell}_{j_t}(\boldsymbol{\theta}^t) - \nabla \hat{\ell}(\boldsymbol{\theta}^t)\|_2^2 \right] \\
&= \mathbb{E} \left[\|\nabla \hat{\ell}_{j_t}(\boldsymbol{\theta}^t) - \nabla \ell_{j_t}(\boldsymbol{\theta}^t) + \nabla \ell_{j_t}(\boldsymbol{\theta}^t) - \nabla \hat{\ell}(\boldsymbol{\theta}^t)\|_2^2 \right] \\
&\leq 2\mathbb{E} \left[\|\nabla \ell_{j_t}(\boldsymbol{\theta}^t) - \nabla \hat{\ell}(\boldsymbol{\theta}^t)\|_2^2 \right] + 2\mathbb{E} \left[\|\nabla \hat{\ell}_{j_t}(\boldsymbol{\theta}^t) - \nabla \ell_{j_t}(\boldsymbol{\theta}^t)\|_2^2 \right] \\
&\leq 4\sigma^2 + \frac{6C}{\sqrt{w}}.
\end{aligned}$$

□

D Additional Technical Details and Numerical Results

In this section, we present technical details that were omitted from the main paper for space. We used the following *signal-to-noise ratio (SNR)* [21, 91] in dB for quantitatively comparing different algorithms

$$\text{SNR}(\hat{\mathbf{x}}, \mathbf{x}) = \max_{a, b \in \mathbb{R}} \left\{ 20 \log_{10} \left(\frac{\|\mathbf{x}\|_2}{\|\mathbf{x} - a\hat{\mathbf{x}} + b\|_2} \right) \right\}, \tag{30}$$

where $\hat{\mathbf{x}}$ and \mathbf{x} represents the noisy vector and ground truth respectively, while the purpose of a and b is to adjust for contrast and offset. We also used the *structural similarity index measure (SSIM)* [92] as an alternative metric. All the experiments in this work were performed on a machine equipped with an Intel Xeon Gold 6130 Processor and eight NVIDIA GeForce RTX 2080 Ti GPUs.

As stated in [33, 35] and other DEQ work, using acceleration can reduce computational costs during both training and inference time and lead to improvement of empirical performance at inference. Here, we focus

Table 4: Average SNR (dB) for different pre-trained CNNs on MRI test images. Note that the ‘‘AWGN denoising’’ performance is for noise level $\sigma = 5$ and the ‘‘Time (ms)’’ presents the runtime of evaluating $R_\theta(\mathbf{x})/\nabla_{\mathbf{x}}R_\theta(\mathbf{x})$ on images of size 320×320 .

Model	DnCNN	Tiny U-Net	U-Net
SNR(dB)			
AWGN denoising	30.30	30.36	30.41
RED (Nesterov)	26.37	26.35	26.42
RED (Anderson)	25.44	25.46	25.51
Time (ms)	12.22 / 31.74	1.65 / 11.48	1.88 / 32.84

on the final image reconstruction performance for denoising based step-descent RED (SD-RED) by using two different fixed-point acceleration methods, namely Anderson acceleration and Nesterov acceleration. The detailed instructions of using Anderson acceleration is publicly available with tutorials ². The Nesterov acceleration for RED (DEQ) and RED (Denoising) can be summarized as

$$\begin{aligned} \mathbf{x}^k &= \mathsf{T}_\theta(\mathbf{s}^k) \\ c_k &= (q_{k-1} - 1)/q_k \\ \mathbf{s}^k &= \mathbf{x}^k + c_k(\mathbf{x}^k - \mathbf{x}^{k-1}), \end{aligned}$$

where the value of $q_k = 1/2(1 + \sqrt{1 + 4q_{k-1}^2})$ is adapted for better PSNR performance. The average SNR (dB) values for RED (Anderson) and RED (Nesterov) using different CNN denoisers on the MRI images are presented in Table 4. We empirically observe that the RED with Nesterov acceleration led to better reconstructions in terms of SNR. For the forward pass iterations, we equip ODER, RED (Denoising), RED (Unfold) and RED (DEQ) with Nesterov acceleration for all experiments used in this work. We utilize Anderson acceleration for the backward pass for both ODER and RED (DEQ). We limit the number of backward pass iterations to 50 for efficiency considerations for all three imaging applications. The number of forward passes is presented in each imaging modality sub-section, respectively. Followed by [35, 76], we additionally set the convergence criterion (relative norm difference between iterations) as

$$\frac{\|\mathbf{x}^{k+1} - \mathbf{x}^k\|_2}{\|\mathbf{x}^k\|_2} < \epsilon,$$

where $\epsilon > 0$. In forward passes, We set $\epsilon = 10^{-3}$ for ODER and RED (DEQ), while we set stopping criterion of backward passes to $\epsilon = 10^{-2}$ for ODER and RED (DEQ).

We additionally tested three network architectures including DnCNN [12], U-Net [4] and tiny U-Net [70]. The DnCNN network has seventeen layers, including 15 hidden layers, an input layer, and an output layer. The tiny U-Net is a simplified variant of the normal U-Net with less trainable parameters. In specific, the CNN consists of four scales, each with a skip connection between downsampling and upsampling. These connections increase the effective receptive field of the CNN. The number of channels in each layer are $\{32, 64, 128, 256\}$. We make two additional modifications to the tiny U-Net. First, we drop out the second group normalization (GN) [90] at each composite convolutional layers. Second, we add spectral normalization to each layers for more stable training and better Lipschitz constrain of the neural network. It is worth to note that spectral normalization is a widely used method for Lipschitz constrained neural network, and it is *not* our aim to claim any algorithmic novelty with respect to it. In Table 4, we present the denoising performance on AWGN removal with noise level $\sigma = 5$ and the run time of calculating $R_\theta(\mathbf{x})/\nabla_{\mathbf{x}}R_\theta(\mathbf{x})$ with respect to a 320×320 image. Overall, the traditional U-Net architecture achieves the best denoising and reconstruction performance, but requires more time per iterate than tiny U-Net. As a result, we implement traditional U-Net denoiser for RED (Denoising), and we equip ODER, RED (DEQ) and RED (Unfold) for the same tiny U-Net architecture in order to decrease per-iteration computation costs during training.

²Anderson acceleration for DEQ was introduced at <http://implicit-layers-tutorial.org/>.

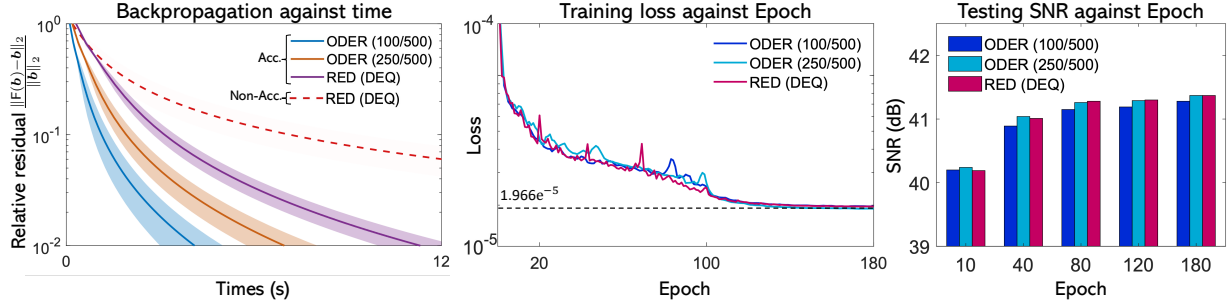


Figure 5: Numerical Illustration of ODER on IDT for two minibatch sizes $w \in \{100, 250\}$. The result for RED (DEQ) with $b = 500$ is also provided for reference. The left figure shows how ODER improves the efficiency of the backward pass of RED (DEQ) by reducing the per-iteration complexity of the measurement matrix. The middle figure plots the loss against the epoch number evaluated on the training set. The right figure plots the SNR (dB) achieved at different epochs for ODER evaluated over the testing set. This figure highlights that by using minibatches $1 \leq w \leq b$, ODER improves per-iteration complexity and matches the same final imaging quality achieved by RED (DEQ).

Table 5: Average SSIM values for IDT image recovery on testing images from [77].

Method	Input SNR (dB)		
	15	20	25
TV	0.9810	0.9829	0.9835
U-Net	0.9811	0.9831	0.9836
ISTA-Net+	0.9809	0.9833	0.9841
SGD-Net (100)	0.9832	0.9859	0.9866
RED (Denoising)	0.9831	0.9852	0.9866
ODER (100)	0.9834	0.9875	0.9889
ODER (250)	0.9846	0.9878	0.9891
RED (DEQ)	0.9845	0.9879	0.9890

In Fig. 4, we report the empirical evaluation of the Lipschitz constant η of T used in our simulations and stated in Lemma 1 on the testing images from all three inverse problems in the main manuscript. We plot the histograms of values $\eta = \|T(\mathbf{x}^{k-1}) - T(\bar{\mathbf{x}})\|_2 / \|\mathbf{x}^{k-1} - \bar{\mathbf{x}}\|_2$, and the maximum value of each histogram is indicated by a vertical bar with the frequency of $\eta > 1$, providing an empirical upper bound on the values of η . Note that despite the numerical limitations of current spectral normalization techniques, they still provide a useful tool to ensure stable convergence.

D.1 Additional Details and Validations for IDT

We follow the experimental setup in [21, 43, 65] to generate the measurement matrix and simulated images for IDT³. In specific, the simulated images are assumed to be on the focal plane $z = 0\mu\text{m}$ with LEDs located at $z_{\text{LED}} = -70\text{mm}$. The wavelength of the illumination was set to $\lambda = 630\text{nm}$ and the background medium index was assumed to be water with $\epsilon_b = 1.33$. We generated $b = 500$ intensity measurements with $40\times$ microscope objectives (MO) and 0.65 numerical aperture (NA). Followed by [65], we assume real permittivity function, and our implementation stores each \mathbf{A}_i as two separate arrays for phase and absorption. In addition, each matrix is stored in the Fourier space to reduce the computational complexity of evaluating convolutions. This result in the storage of complex valued arrays for each, consisting of pairs of single precision floats for every element when training ODER/RED (DEQ). Thus, the shape of each measurements and measurement

³The code is publicly available at <https://github.com/bu-cisl/High-Throughput-IDT>

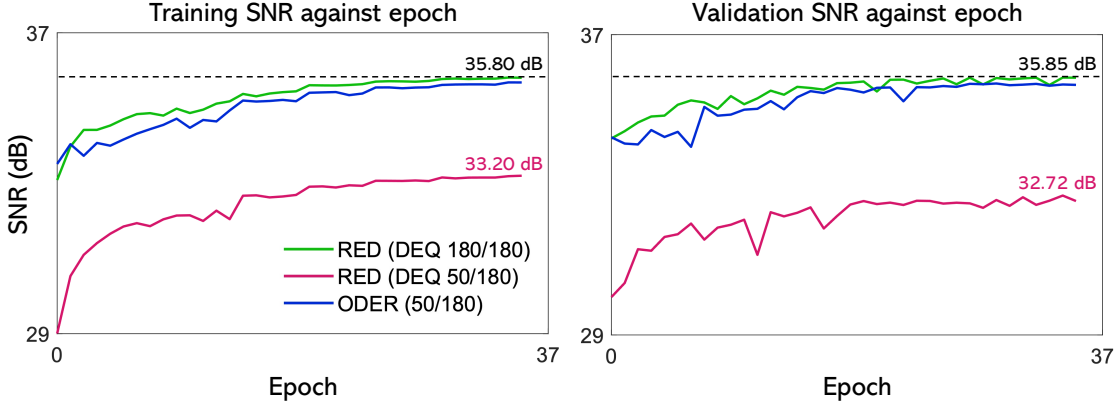


Figure 6: Average SNR of ODER and RED (DEQ) on the training and validation images of sparse-view CT are plotted against the training epoch for a fixed per-iteration measurement budget. The total number of projection views is $b = 180$. Under the same per-iteration memory complexity, the training of ODER achieves a significantly higher SNR than RED (DEQ) when the budget is limited to 50 projection views at per-iterate due to its ability to randomly cycle through the full dataset.

operators in full batch RED (DEQ) for reconstructing one slice is $1 \times 416 \times 416 \times 500 \times 2$. A detailed discussion on the IDT forward model is available in [21, 43].

We train ODER and RED (DEQ) with the initialization $x_0 = \mathbf{A}^H \mathbf{y}$, where \mathbf{A}^H denotes the conjugate transpose. For both ODER and RED (DEQ) during training, we fix the step-size parameter and regularization parameter to $\gamma = 5 \times 10^{-3}$ and $\tau = 4$, respectively. The learning rate of ODER/RED (DEQ) is set in two stages. In the first 100 epochs, we adopt the cyclic learning rate policy [93], where the policy cycles the learning rate between 0.05 and 0.16 with exponentially decay to 0.9998. In stage 2, the learning rate was gradually reduced by a factor of 0.6 every 50 epochs. The number of total training epochs was 200. We set the same forward pass initialization x^0 in ODER for all reference methods. In these experiments, we set the number of forward pass iterations in ODER/RED (DEQ) to $K = 80$, and we set the steps in RED (Denoising) and RED (Unfold) to $K = 100$ and $K = 9$, respectively.

Table 5 reports average SSIM values obtained by ODER and other baselines. Fig. 5 presents quantitative evaluation of ODER on IDT for two minibatch sizes $w \in \{100, 250\}$ against RED (DEQ) using the full-batch of $b = 500$ measurements. Specifically, Fig. 5 (left) presents the empirical acceleration of ODER backward pass over that of RED (DEQ) due to the reduction in the computation complexity of data-consistency blocks at each iteration. Fig. 5 (middle) illustrates the loss against the epoch number on the training set, while Fig. 5 (right) presents the SNR achieved at different epoches for different values of w evaluated over testing set. Fig. 7 provides additional visualizations of IDT reconstruction produced by ODER and other reference methods.

D.2 Additional Details and Validations for CT/MRI

Sparse-view CT. For the CT images, we train ODER by using the filtered backprojection (FBP) initialization $x^0 = \mathbf{A}^H F \mathbf{y}$. We use the Hann filter for FBP reconstruction. We set the number of forward pass steps in ODER/RED (DEQ) to $K = 180$, and we use Adam with training minibatch size 4 and weight decay 1×10^{-7} . For ODER and RED (DEQ), we fixed the step-size to $\gamma = 1.25 \times 10^{-3}$ and regularization parameter to $\tau = 3$. The learning rate starts from 3×10^{-4} and is halved at epoch 15, then gradually reduced by a factor of 0.6 every 5 epochs. The number of total training epochs is 35. It is worth to note that we equally divided the full projection views $b \in \{90, 120, 180\}$ into 5 non-overlapping chunks, each with size of $\{18, 24, 36\}$ views, respectively. At every iterations, the corresponding ODER model with $w/b \in \{30/90, 40/120, 50/180\}$ randomly picks a subset of $\{6, 8, 10\}$ from each chunk for the data-consistency block calculation. This leads to better empirical reconstruction improvement for ODER. Similarly, we set the number of forward pass

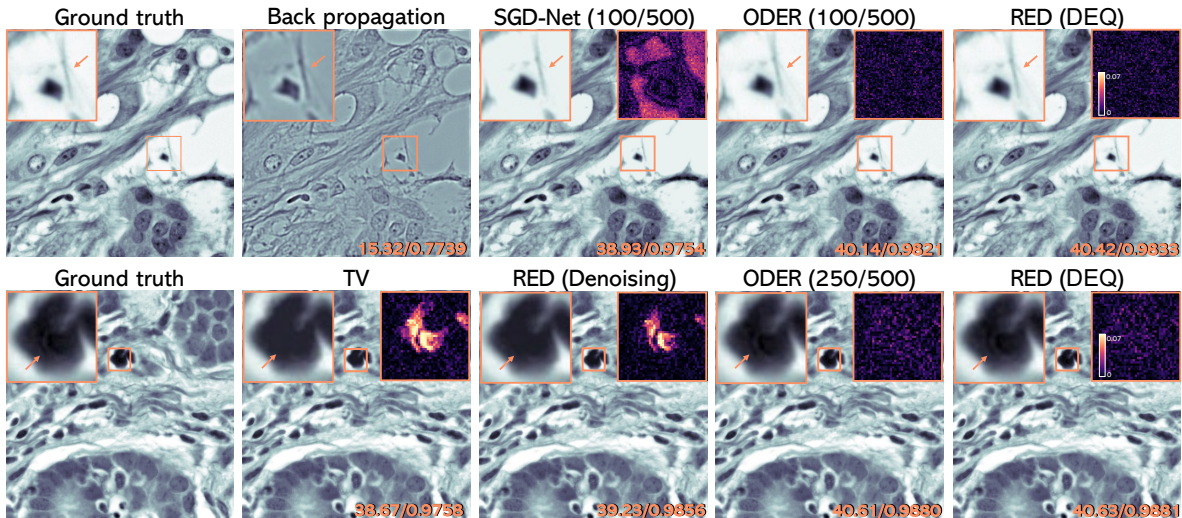


Figure 7: Quantitative evaluation of several well-known methods on IDT under noise corresponding to input SNR of 20 dB. The total number of IDT measurements in this experiment is $b = 500$. RED (DEQ) corresponds to the full batch architecture that uses all the measurements at every step. Each image is labeled with its SNR (dB) and SSIM values with respect to the original image. The yellow box provides a close-up with a corresponding error map provided on its right. Note the similar performance of ODER and RED (DEQ), and the improvement over RED (Denoising) /RED (Unfold) due to the usage of DEQ learning. Best viewed on a digital display.

iterations in RED (Denoising) and RED (Unfold) to $K = 150$ and $K = 7$, respectively.

Fig. 6 compares the average reconstruction SNR of ODER and RED (DEQ) for a fixed periteration measurement budget on sparse-view CT. The total number of projection views is $b = 180$. The batch algorithm RED (DEQ 50/180) and ODER with ($w = 50$) are allowed to use only 50 projection views at per iterate. This means that in each figure both RED (DEQ 50/180) and ODER with ($w = 50$) have the same per-iteration computational complexity. Empirically, we observe that ODER outperforms RED (DEQ 50/180) by around 3 dB on the validation set under the same per-step memory complexity and matches the performance of RED (DEQ 180/180). In Fig. 8 (top), we provide additional visualizations of the solutions produced by ODER/RED (DEQ) and various baseline methods considered in our work.

Parallel MRI. For the MRI images, we train ODER/RED (DEQ) by using the zero-filled reconstruction as initialization x^0 . For the 2D MRI images, we set the number of iterations in ODER/RED (DEQ) to $K = 200$, and we use Adam with training minibatch size 16 and weight decay 2×10^{-7} . We fixed the step-size to $\gamma = 1.2$ and regularization parameter to $\tau = 0.05$ for both ODER and RED (DEQ). The learning rate starts from 1×10^{-4} and is gradually reduced by a factor of 0.6 every 10 epochs. The number of total training epochs is 40. In these experiments, we set the number of forward pass iterations in RED (Denoising) and RED (Unfold) to $K = 200$ and $K = 25$, respectively. For the 3D MRI volumes, we set the number of steps in ODER/RED (DEQ) to $K = 400$, and we use Adam with training minibatch size 4 and weight decay 1×10^{-6} . We fixed the step-size to $\gamma = 1.25$ and regularization parameter to $\tau = 0.01$ for both ODER and RED (DEQ). The learning rate starts from 5×10^{-5} and is gradually reduced by a factor of 0.65 every 10 epochs. The number of total training epochs is 100. Similar to sparse-view CT, we equally divided the number of coil sensitive maps $b = 96$ into 4 non-overlapping chunks, each with size of 24 coils, respectively. At every iterations, the corresponding ODER model with $w = 48$ randomly picks a subset of 12 from each chunk for the data-consistency block calculation. For the 3D MRI volumes, we set the number of forward pass iterations in RED (Denoising) and RED (Unfold) to $K = 400$ and $K = 20$, respectively. Fig. 8 (bottom) reports the comparison on medical brain images for CS-MRI with under-sampling ratio of 10%.

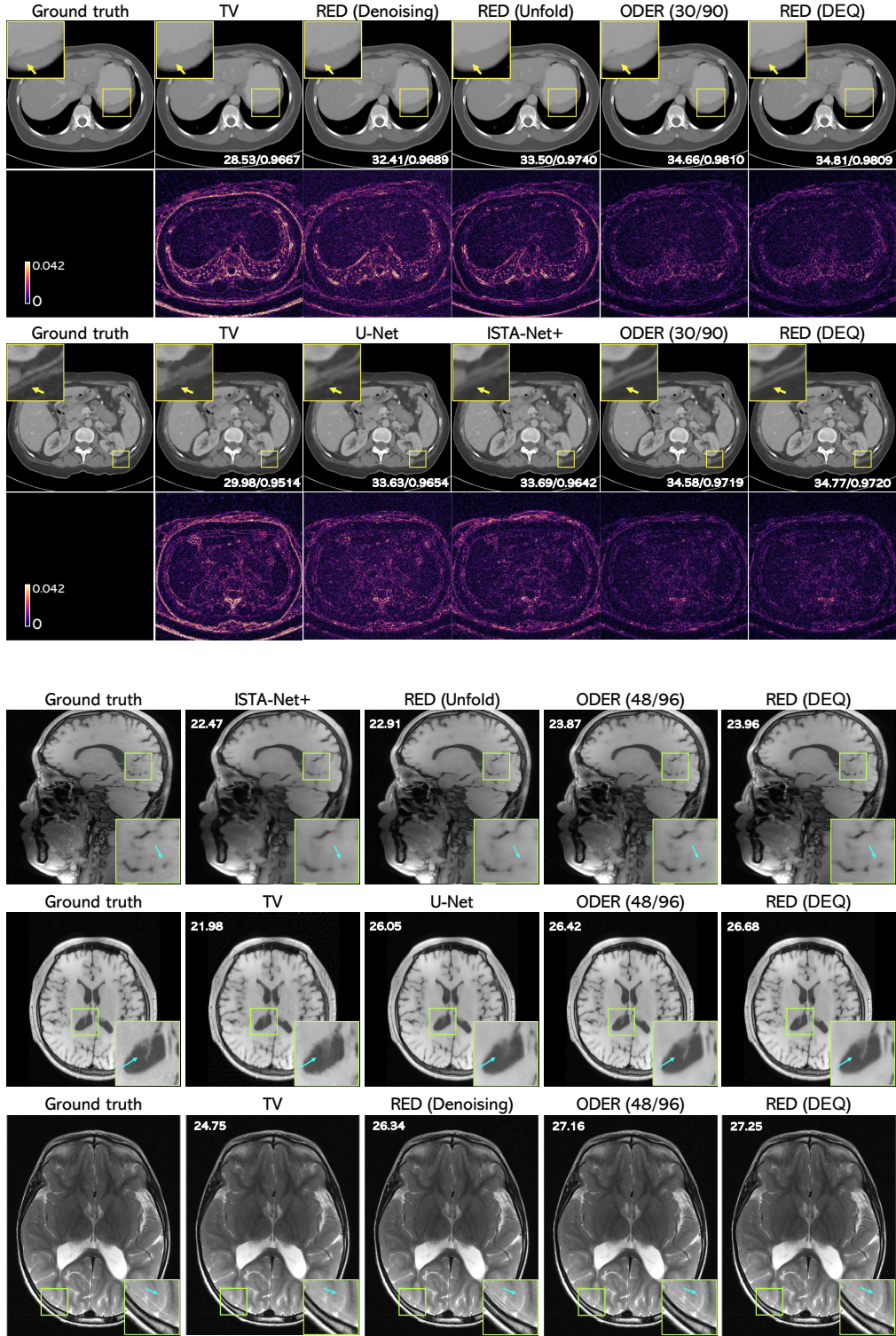


Figure 8: Visual evaluation of several well-known methods on two imaging problems: (top) Reconstruction of sparse-view CT from $b = 90$ projection views. Each image is labeled with the corresponding SNR (dB) and SSIM values. The figures below are the error residual images to the ground truth; (bottom) Reconstruction of brain MRI images from its radial Fourier measurements at 10% sampling with $b = 96$ simulated coil sensitivity maps. Best viewed on a digital display.